ABSTRACT

Title of Document: CHARACTERIZATION OF EXFOLIATED GRAPHITE AND LATEX COMPOSITE AS TEMPERATURE SENSORS TO PRODUCE THERMAL IMAGES

Elizabeth Ann Sauerbrunn, Master of Science, 2014

Directed By: Professor Hugh A. Bruck
Department of Mechanical Engineering

Temperature sensing is crucial in spacecraft to ensure all systems remain within operating temperatures. Sensing over an area would allow thermal management systems to effectively see the temperature profile in real time, which is not being done with thermocouple and RTD systems used today.

The resistance response as a function of temperature for exfoliated graphite and latex composite sensors was investigated. The effect of the substrate CTE and the EG loading level were observed and 30 wt% EG sensors were calibrated on a carbon fiber substrate. Above room temperature, the percent resistance change and temperature relationship is linear, while below room temperature the relationship is exponential. The resistance response from twelve sensor grids was converted into a temperature field to produce thermal images over a surface. These temperature profiles were compared to thermal simulation data, proving that the sensor grids successfully mapped the proper temperature patterns.

CHARACTERIZATION OF EXFOLIATED GRAPHITE AND LATEX COMPOSITE AS TEMPERATURE SENSORS TO PRODUCE THERMAL IMAGES

By

Elizabeth Ann Sauerbrunn

Thesis submitted to the Faculty of the Graduate School of the
University of Maryland, College Park, in partial fulfillment
of the requirements for the degree of
Master of Science
2014

Advisory Committee:
Professor Hugh A. Bruck, Chair and Advisor
Professor Elisabeth Smela
Associate Professor Miao Yu

Acknowledgements

I am grateful for the guidance and support of my advisor, Dr. Bruck, through my three years of work under him as an undergraduate research assistant and a BS/MS student. The knowledge and experience I have gained under your guidance has become invaluable. I also thank Dr. Smela for acting as an informal co-advisor, honing my skills for the scientific method and ensuring that all experiments were conducted thoroughly. To my final committee member, Dr. Yu, thank you for your insight and suggestions that solidified the direction of this research. Thank you to all three professors for taking the time to work with me and teach me through this process.

Outside of academia I received significant help and guidance from my superiors in the Thermal Engineering Branch (Code 545) at NASA's Goddard Space Flight Center. Jeff Didion served as my NASA mentor and was instrumental in making this research a reality. I thank you for the years of leadership and opportunities that you provided to me along the way. Frank Robinson and Mario Martins were also huge helps and took the time to get me acquainted with the thermal engineering field. Your willingness to teach me, answer questions, and patience while I learned are very much appreciated. I also thank the rest of Code 545 for welcoming me and making my experience at Goddard an exciting one.

A huge thank you to all of my fellow graduate students in the MML and AML; specifically Sandip Haldar, Ariel Perez-Rosado, Graeme Fukuda, Luke Roberts, Prakhar Singh, Chris Bilger, and Alex Holness. You all made the entire graduate school experience a fun and rewarding one.

To my parents, Linda and Steve Sauerbrunn, thank you for always supporting me and encouraging me to follow my dreams – I could not have gotten this far without you. To my sisters, Christine and Stephanie Sauerbrunn, your source of entertainment was always a nice break from the stresses of school and much appreciated. To my Oma, Shirley Hoeflich, you have always been a source of inspiration and a constant reminder of the importance of education. To my boyfriend, Ron Kayea, your love and support over the past five years has gotten me through more than I thought possible. To my fellow Terps and best friends – Sarah, Haley, Hannah A, Hannah B, Ashley, Lauren, and Erin – you all are the best friends I could have asked for and made my time at Maryland the best.

Finally, this research would not have been possible without NASA Headquarters their generous NASA Science and Technology Research Fellowship (NSTRF) awarded to me and the University of Maryland.

Table of Contents

List of Tables

List of Equations

List of Figures

List of Abbreviations

CB	Carbon black
CF	Carbon fiber
CNT	Carbon nanotube
CTE	Coefficient of thermal expansion
DAQ	Data acquisition
EDPM	Ethylene propylene diene monomer
EG	Exfoliated graphite
EVA	Ethylene vinyl acetate
FEA	Finite element analysis
FO	Fiber optic
LEO	Low earth orbit
NASA	National Aeronautics and Space Administration
NR	Natural rubber
NTC	Negative temperature coefficient
PDMS	Polydimethylsiloxane
PMMA	Polymethyl methacrylate
PTC	Positive temperature coefficient
RT	Room temperature
RTDs	Resistance temperature detectors
STRs	Space technology roadmaps
TA	Technology area
TPS	Thermal protection system
UHMWPE	Ultra high molecular weight polyethylene

Chapter 1 – Introduction

1.1 Motivation and Background

Currently, thermal management systems on sounding rockets or satellite walls, such as a base plate, are dependent on conventional temperature sensors – thermocouples, thermistors, and resistive temperature detectors (RTDs) – that are physically attached onto the plates. They rely on strategically placed sensors to read temperatures on any given surface. However, thermocouple readings are susceptible to error due to highly transient localized heating and cooling effects, such as thermal spikes and large gradients, that puts the system at risk of overheating [1]. If a hotspot occurs where there is no thermocouple, the thermal management system will never know there is a problem until it is too late. A grid of conductive nano-filled polymer composites can be used as a "nervous system", allowing the thermal management system to self-sense and be able to map its temperature profile in real-time.

The National Aeronautics and Space Administration (NASA) has published a number of documents called Space Technology Roadmaps (STRs) that identify fourteen technology areas (TAs) that represent the agency's top technical challenges. The Thermal Management Systems STR, also known as TA14, details research goals and timelines that are needed to advance the thermal systems in spacecraft [2]. It is clearly stated in this STR that the development of sensors that can measure field data is one such desired research goal. This research aims to study a nano-enhanced composite sensor and its response to temperature fields over an area to potentially serve as the advanced sensor identified in TA14.

1.2 Research Goals

The goal of this project is to fully characterize exfoliated graphite (EG) and latex composite sensors as temperature sensors for use in space applications – specifically in thermal management systems. In order to accomplish this, the sensors must first be calibrated based on the resistance response as a function of temperature. This calibration response, which should be dependent on the substrate's coefficient of thermal expansion (CTE) and the weight percent of EG in the sensor, also referred to as loading level, will be used to calculate temperature based on the recorded resistance response.

Grids of these sensors will be used to measure temperature changes over an area when a non-uniform temperature field is applied. Temperature contour plots will be generated using the calibration data and the sensor's resistances, proving that thermal imaging over a surface is possible with EG and latex composite sensors. This data will be validated by comparing the experimental results with theoretical temperature fields obtained by finite element analysis (FEA).

1.3 My Contributions

Through this research, I will be expanding on the knowledge established by Mark Kujawski on the EG and latex composite materials [3]. The initial research focused on the material's response to mechanically induced strain, so my research aims to fill in the holes left by Kujawski in regards to the temperature response of these sensors. Through this investigation, I will further the understanding and knowledge of nano-filled conductive polymer composite temperature dependencies. Specifically, I will thermally characterize the EG and latex composite material for the first time.

Making twelve sensor grids and producing thermal images over a surface will be the first time, to our knowledge, that such data has been produced from these types of sensors.

Chapter 2 – Literature Review

In order to develop temperature sensors out of nano-enhanced conductive polymers, the previous research on such materials must be understood. Studying the applications for these sensors is also important so that the current temperature measurement systems can be improved upon. The following subsections investigate current spacecraft temperature measurement systems and the types of nano-enhanced polymers that have already been developed into various sensors types.

2.1 Temperature Sensing in Spacecraft

Accurately sensing and controlling temperatures throughout a spacecraft is arguably the most crucial function on board. Without thermal control, all of the important and sensitive electronic equipment will not function as intended. The three main sources of heat in Low Earth Orbit (LEO) are shown in Figure 1 and include solar radiation, reflection of the solar radiation off of the earth (albedo), and radiation from the earth itself.

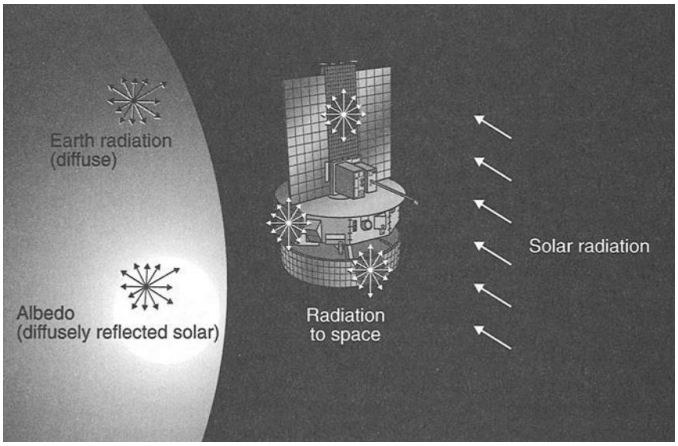

Figure 1 – Thermal environment in space due to albedo and radiation sources [4].

Solar radiation is the largest source of heat for a LEO satellite and averages to about 1367 $\frac{W}{m^2}$, otherwise known as the solar constant [4]. This large amount of heat

from the sun and the frigid 3 Kelvin of deep space [5] makes maintaining strict thermal limits within the spacecraft a difficult, yet crucial, task. Typical internal temperatures that must be maintained can be found in Figure 2.

Equipment	Operational	Survival
Avionics Baseplates	–20 to 60	–40 to 75
Batteries	10 to 30	0 to 40
Hydrazine Fuel	15 to 40	5 to 50
Solar Arrays	–150 to 110	–200 to 130
Antennas	–100 to 100	–120 to 120
Reaction Wheels	–10 to 40	–20 to 50
Typical Temperature Requirements °C		

Figure 2 – Typical temperature requirements for onboard spacecraft systems that must be maintained by the thermal control system [5].

Although passive thermal control methods such as surface finishes, blankets, radiators, and heat pipes are effective, active control is needed to supply or remove heat from a given area [4]. This active control is dependent on the thermal sensing data collected. Current methods of sensing temperature on spacecraft include extensive use of thermocouples, RTDs, and thermistors. These sensors are strategically placed at predetermined locations based on predicted thermal points of interest.

NASA has identified the need for advances in ultra-light-weight thermal protection system (TPS) sensor systems measuring temperature and strain, among others quantities of interest in their Technology Area 14: Thermal Management Systems Roadmap [2]. These advances in on-board sensor systems not only benefit space applications but have “major impacts” on other areas of national need, including sectors such as engineering and industry, science and technology, and home land security and the Department of Defense. When the dependencies and collaborations

between sensor systems and other technology areas were listed, only Technology Areas 3 (TA3: Space Power & Energy Storage Systems) and 4 (TA4: Robotics, Tele-Robotics, & Autonomous Systems) were included, leaving out TA10 (Nanotechnology) and TA12 (Materials, Structural & Mechanical Systems, & Manufacturing). Achieving the goals of this project would not only satisfy NASA's need for thermal sensor system advances but would also incorporate additional Technology Areas such as nanotechnology and materials research, taking advantage of other work being conducted throughout NASA.

Some advances have already begun to take place within the sensor system need, including distributed fiber optic (FO) temperature sensors [2,6] and solar cells acting as capacitive temperature sensors [7]. Although not being extensively researched for space applications, conductive polymer composites have been thoroughly studied and have been developed into various sensor types [3,8-14]. The knowledge and range of materials available to make conductive polymer composites shows that these materials are a plausible route for the development of these temperature sensors. One major issue with polymers in space is that most organic materials will outgas in vacuum and are strictly prohibited in many applications because the outgassed molecules can contaminate crucial surfaces and instruments within the spacecraft [5]. This issue can be avoided by properly enclosing the materials, not allowing the outgassing molecules to interfere with the rest of the spacecraft functions.

2.2 How Thermocouples, RTDs, and Thermistors Work

Some of the most common temperature sensor devices used today includes thermocouples, RTDs, and thermistors. Each device has a temperature dependent electrical output. The theories for each are presented and compared in this section.

Thermocouples are temperature sensing devices where two wires of dissimilar metals are connected to each other at a junction. This difference between metals creates a voltage potential, called a Seebeck voltage, that is dependent on temperature and creates a thermoelectric current [15]. A Type T thermocouple, widely used in space applications, consists of a pure copper wire and a constantan wire. Constantan is a copper alloy containing approximately 43% nickel while the rest is copper [15]. These thermocouples can measure temperatures within 1% accuracy between -190 °C and 380 °C. As mentioned in Section 1.1, thermocouple responses can be false if the temperature gradient over the junction is too high, leaving room for error in thermal control systems. This is because if the junction experiences a temperature gradient, one portion will produce a larger current than the other, effectively averaging the temperature over the junction.

On the other hand, RTDs are devices whose resistance is a function of temperature. A fine coil of a pure noble metal wire is wrapped around an insulating core with a low CTE [16]. The most commonly used metal in these sensors is platinum, which can be used in operating temperatures between -220 °C and 850 °C. Generally, the metals used in RTDs are positive temperature coefficient (PTC) materials; meaning resistance and temperature are directly proportional within the operating temperature

range. The intrinsic electrical resistivity (ρ_i) of pure metals as a function of temperature (T) is commonly described by the Bloch-Grüneisen equation found in Equation 1 [17].

Equation 1 – Bloch-Grüneisen equation [17]

$$\rho_i(T) = \frac{C}{M\theta}\left(\frac{T}{\theta}\right)^5 J_s\left(\frac{\theta}{T}\right)$$

The constants represent: T – temperature (K), θ – Debye temperature of metal, J_s – transport integral, C – constant of the metal. The constant, C, is positive for noble metals like the platinum used in most RTDs, defining the PTC property of these sensors. The resistance repeatability of pure metals make RTDs a reliable choice, however, the brittle core that the metal is coiled around causes RTDs to be quite fragile. The coil of platinum provides a more accurate resistance response compared to deposited platinum because the coiled metal experiences less strain.

Thermistors, much like RTDs, are sensors with a temperature dependent resistance. The difference between the two is that unlike the RTDs, most thermistors are negative temperature coefficient (NTC) due to the semiconductor materials that yield an inversely proportional resistance and temperature relationship. The resistances of semiconductor materials that are used to make thermistors are often modeled by the Steinhart-Hart equation found in Equation 2.

Equation 2 – Steinhart-Hart equation [18]

$$\frac{1}{T} = A + B\log R + C\,(\log R)^3$$

The constants represent: T – temperature (K), R – resistance (ohms), A, B, and C – Steinhart-Hart coefficients. These coefficients dictate the resistance response and are published by thermistor manufacturers. Thermistors can be PTC materials but NTC thermistors are more commonly used for temperature measurements. These NTC

sensors consist of semiconductor materials containing manganese, cobalt, nickel, and copper [16] that can measure between -50 °C to 250°C. Thermistors have the smallest operating temperature range out of the three meaning the applications they can be used for are not as versatile.

There are obviously effective and trusted temperature measurement devices on the market, but they all come with different pros and cons. The gradient issue with thermocouples, the fragile cores in RTDs, and the smaller operating range of thermistors all pose problems. In addition, none of these sensors have the ability to sense temperature over an area. Temperature fields can be measured over an area optically using thermal imaging cameras. This option is not viable for the use in spacecraft due to volume and mass limitations. Although these three measurements methods are widely used in thermal management systems and in other industries as well, there is still room for improvement.

2.3 Conductive Polymer Composites as Sensors

Many different conductive nano-fillers and polymer matrices were considered during the sensor development process for this research. A conductive composite sensor was initially of interest because of the inherent benefits of composite materials yield. Composite materials can be designed and engineered to yield desired mechanical, electrical, and chemical properties. In order for the sensors to work, the material must be able to carry a current so electrical conductivity was a priority in material selection. In order for the sensor to detect temperature changes, the material also had to be thermally conductive so that the heat could be effectively transferred through the sensor.

Some popular conductive nano-particles used in these composites include carbon nanotubes (CNTs) [8,9,13,19-23], carbon black (CB) [8,24,25], short carbon fiber (SCF) [24], and graphite based nano-particles [3,10,11,20,21,26-31]. Two widely studied polymer matrices for these composites are thermoset materials such as epoxy [20,32-36] and polydimethylsiloxane (PDMS) [3,9] and thermoplastic materials such as rubbers [3,10,11,24,37], polymethyl methacrylate (PMMA) [8], and ultra-high-molecular-weight polyethylene (UHMWPE) [25]. A comprehensive list of filler and matrix combinations can be found in Spitalsky et al. Conductive polymer composites have been used to measure quantities such as strain [3,8,10,11] and temperature [9,12].

In order to ensure a nano-filled polymer composite is able to conduct electrons, the percentage of nano-filler must be above the percolation threshold. When polymers are filled with conductive nano-particles, there must be enough randomly dispersed particles so that they are touching throughout the material. This connection creates electrical networks through the material to conduct electrons. The percolation threshold is the point at which there are enough particles touching through the matrix to make the bulk material electrically conductive [38]. The relationship between the conductivity and the filler percent near the percolation threshold has been observed as a power law relationship. This means that small deviations above the threshold can significantly change the conductivity of the material. This concept is kept in mind throughout the sensor development process.

2.4 Temperature Dependence of Nano-Filled Polymers

Changes in the conductivity of these particle-filled polymers have been observed due to mechanically induced strain [3,8,10]. The number of conductive

pathways between particles decreases and resistance increases as the material deforms. Similarly, changes in conductivity of some conductive polymer composites have been recorded due to changing thermal loads [12,28]. The material's temperature dependent conductivity can be categorized as either a PTC or an NTC. These responses are dictated by both the polymer matrix characteristics and the particle-filler material properties.

Das et al. studied the temperature behavior of CB filled and SCF filled rubbers such as ethylene vinyl acetate (EVA) and ethylene propylene diene monomer (EDPM) [24]. They reported that the SCF filled materials showed a PTC with conductivity but the CB filled polymers showed NTC behavior. The PTC behavior observed with the SCF filler has been associated with the difference between the thermal expansions of the fibers and the polymer matrix. The electrical network that is established between the particles above the percolation threshold begins to breakdown because of this thermal expansion difference since the polymer will expand more than the fiber, reducing the pathways for an electron to travel.

The NTC behavior associated with the CB particles was attributed to other phenomena, however. One explanation was that additional networks between particles could form during heating because of flocculation of the filler particles. This means as the material heats, particles clump together, thus changing and possibly adding conductive pathways. Another explanation was that the emission of electrons between two CB particles in higher temperature would increase the conductivity of the material.

Generally, the overall response will be affected by both the matrix and filler. If they have opposing temperature coefficient properties, one component will dominate

the bulk response depending on the amount of filler in the composite. This phenomenon will become crucial to understanding the EG and latex material behavior during calibration.

2.5 EG and Latex as Mechanical Strain Gauges

Although there are numerous conductive filler particles that respond to temperature, graphene based nano-platelets have shown promising results [26]. In fact, EG and latex composite sensors have been developed as compliant strain gauges [3,10]. EG particles were used in this development because of how easy and inexpensive it is to obtain when compared to CNTs and other nano-fillers. The benefits of the latex matrix are that no curing is required and the elastomeric nature of the latex allows the sensors to respond to large deformations. Cantilever beam experiments were conducted to characterize the material's strain response and can be found in Figure 3.

Figure 3 – Cantilever beam test on EG and latex strain gauges to determine the calibration coefficient due to strain [unpublished photo from Dr. Smela's research group].

Although temperature dependence was tested by Kujawski initially during the strain gauge development, it was found that the resistance of the composites had little dependence on temperature compared to the resistance response to strain [3]. It is true

that the temperature effect is negligible when the sensor is being deformed, however the temperature dependence was not tested thoroughly without also being strained, and therefore leaving room for investigation.

Since development in 2010, these strain gauges have been used in a number of applications, including the University of Maryland's robotic bird, the RoboRaven [11]. The sensors were applied near the spars of the wings (Figure 4a) to allow the bird to sense the magnitude and location of the wing deformations during flight, simulated in Figure 4b.

Figure 4 – (a) EG and latex sensors on the wing of RoboRaven placed at areas of high strain. (b) Wings in load cell to measure thrust vs. resistance [unpublished photo from Dr. Smela's research group].

Currently, further work is being conducted to optimize the location of the strain gauges and to incorporate the real-time data into the bird's data acquisition system. The intention is that RoboRaven will be able to sense the change in wind forces during flight to compensate the flapping pattern autonomously. This application will benefit from the thermal characterization conducted under this research.

2.6 Latex Material Properties

Latex is an emulsion of natural rubber (NR) molecules in water based liquid and is commonly used in many products that need elastomeric properties.

Understanding the chemical and physical properties of natural rubber and elastomers in general is an imperative step to understand the EG and latex composite as a whole. The properties of latex presented in this section were found in Reference [39] unless otherwise noted.

Polymer materials such as NR consist of long polymer chains that can entangle and crosslink with each other. The level of entanglements and crosslinks determine the material properties such as modulus and CTE. The polymer chain that makes up the NR is cis 1,4-polyisoprene and can be found in Figure 5.

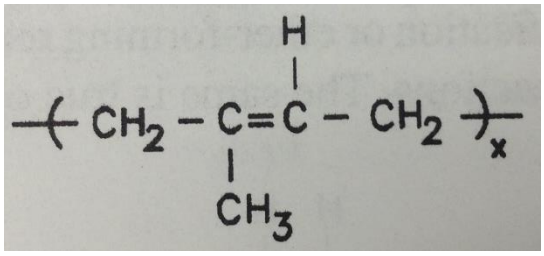

Figure 5 – Natural rubber polymer composition (cis 1,4-polyisoprene) [39].

The geometry of cis-1,4 polyisoprene causes a lower packing density and therefore more free volume between chains when compared to the trans-1,4 polyisoprene varieties. However, due to the higher packing density of the trans-1,4 geometry and the increase in crystallinity, it is a much tougher and stiffer rubber.

Vulcanization is a process in which sulfur is introduced into the NR to harden the rubber to a desired level. The sulfur establishes bonds between the polymer chains, also known as crosslinks. However, if sulfur is not specifically introduced into the latex before it is allowed to cure, the product is then referred to as unvulcanized rubber, simply meaning there are little to no crosslinks. With such few crosslinks, the polymer chains in the NR have more freedom to rotate about the single bonds in the chain. The strength of the unvulcanized NR comes mostly from the chain entanglements and the

few crosslinks that are present. Entanglements are more easily displaced, or labile, at higher temperatures since the chains are more flexible and the net number of anchor points between molecules decreases. The chain movement with temperature causes latex to have a high and varying CTE.

2.7 EG Material Properties

Understanding the properties of graphite will add insight to how the EG will affect the composite sensors being developed. Graphite is sheets of graphene layers that are held together by weak van der Waal forces [10], which can be seen in Figure 6.

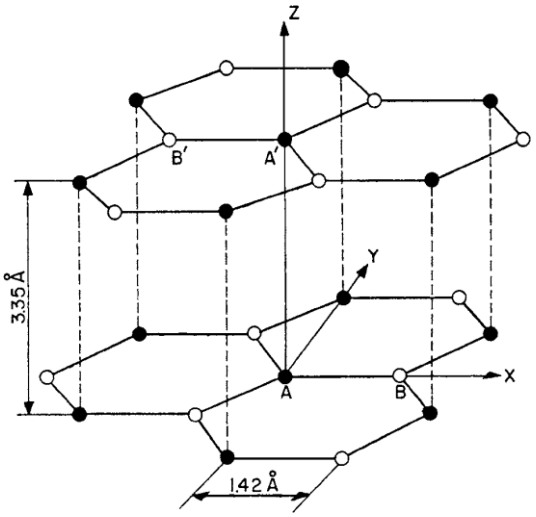

Figure 6 – Lattice structure of graphite showing the weak forces in the z-plane between graphene sheets [40].

The graphene layers that are left after exfoliation and sonication are 1 atom thick sheets of sp^2 hybridized carbon in a hexagonal lattice [10]. Graphene is a zero-band gap semiconductor and inherently is an NTC material [3,40]. As the thermal energy increases, electrons move more easily from one EG particle to the next, causing the resistance to decrease [3]. This is important because assuming the thermal

expansion of the material is negligible, the thermal response of the EG and latex should mimic the NTC response of the EG. However, the expansion of the latex will create a PTC effect. As mentioned before, these forces will oppose each other. It will be crucial to understand at what point each effect will dominate the bulk behavior.

Chapter 3 – Methods and Materials

3.1 Materials

3.1.1 Latex

Latex is a widely used material and is easily obtained. The latex used to make these sensors is sold by Artmolds to make latex casts for mask making. According to the material data sheet, this pre-vulcanized latex has a viscosity described as a pourable paste, has a pH between 9.5 and 10.5, and contains 62% natural rubber (NR) solids [41]. Sulfur-based additives are also sold by the company to adjust the rubber hardness as desired by controlling the crosslink density. Since the latex is used without a hardening agent in this research, it can be assumed that the dried latex is not heavily cross-linked. This means the resultant rubber has a very low Young's modulus and can withstand large deformations. It also means that the polymer chains are relatively free to move when a thermal or mechanical load is applied [39].

This latex is water-based but does contain ammonia to preserve the material's viscosity for longer. When allowed to dry, both the water and ammonia evaporate, leaving the NR solids behind. The percentage of solids in the latex was experimentally tested to verify the 62% reported in the material data sheet. The mass of a small portion of the fresh latex was taken initially and then again after the latex was allowed to dry for two days, experimentally showing 64% NR. The difference between the reported value and the experimental is most likely due to some evaporation during the manufacturing and handling process.

3.1.2 Graphite Flake Exfoliation

The size and shape of the graphene particles are crucial to the conductivity of the composite sensor. The exfoliation of graphite is a simple and inexpensive way to produce the necessary graphene nano-particles needed for these sensors. The same microwave exfoliation process followed by Kujawski et al. [10], originally presented by Falcao et al. [42] and Wei et al. [43], was used for this research.

Acid-washed graphite flake (Ashury Graphite Mills, Inc.) in a glass beaker (Figure 7) was placed in an 1100 W microwave (Kenmore) with a frequency of 2.45 GHz. Forming gas (97% nitrogen and 3% hydrogen) was fed into the microwave for 10 min at a rate of 1 L/min. The microwave was turned on at full power for one minute. The exfoliated graphite particles became worm-like and experienced a volume increase of 200 – 300 times the initial volume [10] during the process as is evident in Figure 8. Figure 9 shows the scanning electron microscope image of an exfoliated graphite particle.

Figure 7 – Acid-washed graphite flake before microwave irradiation [unpublished photo from Dr. Smela's research group].

Figure 8 – Worm-like exfoliated graphite particles after microwave irradiation [unpublished photo from Dr. Smela's research group].

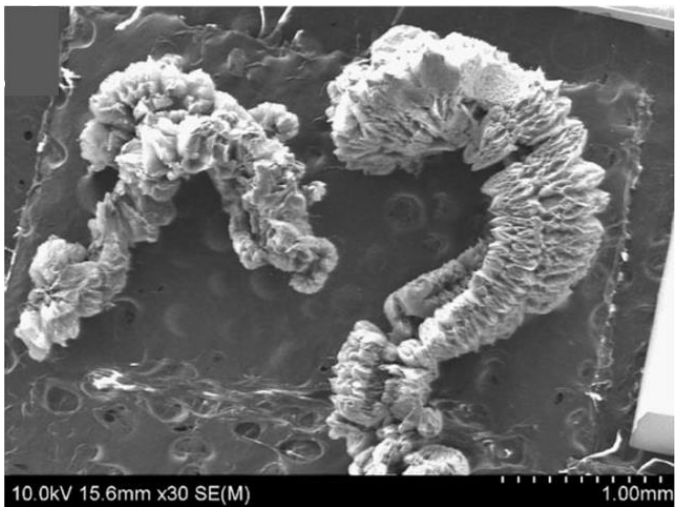

Figure 9 – SEM image of exfoliated graphite particles before sonication [10].

The exfoliated particles were filtered by stirring them into hexane, leaving the particles floating on the top and the denser, unexfoliated flakes at the bottom of the solution. The floating particles were collected from the surface of the hexane and were dried at 150 °C overnight. All of the exfoliated graphite particles used for this research had previously been exfoliated by another student prior to the commencement of this study.

3.1.3 Making the Latex and EG Solution

Test specimens are comprised of a substrate coated first with latex primer and then an aqueous solution of EG and latex. The latex primer (Glidden GRIPPER interior/exterior grey) was used to ensure the surface of the substrate was electrically insulated so that only the resistance of the conductive sensor was read. The EG solution was prepared in 100 mL batches as described previously [10]: 0.754 g of Triton X-100 surfactant (Sigma Aldrich) was added to 101 g of deionized water and placed on a hot plate at 90°C and magnetically stirred at 500 rpm. While still on the hot plate and stirrer (Fisher Scientific), 1.0 g of EG was added over the course of 30 seconds to the

glass container, followed by four drops of Antifoam SE-15 (Sigma Aldrich). The glass container was placed in an ice bath and horn sonicated as described previously [11]: horn sonicator (QSonica, Q700) with a 0.5 inch tip (solid, tip 201) at 100% amplitude. The original sonication time of 19 minutes was changed to approximately 45 minutes to ensure complete EG particle separation.

The composite solution was prepared by mixing the EG solution and the mask-making latex (RD-407, ArtMolds) in ratios depending on the desired EG loading level. This solution was vortex mixed (Fisher Scientific digital vortex mixer) in a vial at 3000 rpm for 30 seconds right side up and again upside down [11]. The lowest EG loading percentage tested was 10 wt%, which is well above the 4 wt% EG percolation threshold found in previous research [3].

Although the theoretical EG percentage of the solution can easily be calculated, the actual percentage can vary because of evaporation during the sonication process. Each new batch of EG solution was tested for the actual concentration of EG. The loss from evaporation in the EG solution was experimentally found by measuring the mass of the aqueous solution initially and again after two days of drying. The EG solution was expected to contain 0.938% solids, but 1.6% - 1.7% solids were experimentally found depending on the batch. Equation 3 and Equation 4 are used to determine the exact EG loading of any sensor given the percent EG solids ($r_{\text{EG solids}}$), percent NR solids in the latex ($r_{\text{NR solids}}$), and the desired total aqueous mass (M_{Total}).

Equation 3 – (a) Dry EG mass calculation, (b) Dry NR mass calculation

$$\text{(a) } M_{\text{dry EG}} = \frac{r_{\text{EG solids}}}{100} * M_{\text{wet EG}}, \quad \text{(b) } M_{\text{dry latex}} = \frac{r_{\text{NR solids}}}{100} * M_{\text{wet latex}}$$

Equation 4 – EG loading calculation system of equations

$$\text{Desired EG loading} = \left(\frac{M_{\text{dry EG}}}{M_{\text{dry EG}} + M_{\text{dry latex}}}\right),\ M_{\text{wet EG}} + M_{\text{wet latex}} = M_{\text{Total}}$$

These equations were inserted into a Matlab code to quickly calculate the masses needed to make the proper EG and latex solution for the desired sensor loading. Table 1 shows the masses needed of the EG solution and latex assuming the EG solution was 1.6% solid, the latex is 64% NR, and the total aqueous mass is 5 grams. This was enough solution to make five two-node sensors.

Table 1 – EG and latex mass for specific EG loading levels

EG Loading %	Liquid EG Solution (g)	Wet Latex Mass (g)
10%	4.0816	0.9184
15%	4.3796	0.6204
20%	4.5455	0.4545
25%	4.6512	0.3488
30%	4.7244	0.2756

3.1.4 Substrates

These sensors were applied to a variety of substrates to observe how the CTE of the substrate affected the resistance response of the sensors. The higher the substrate CTE, the more thermally-induced strain will be applied to the sensor, potentially changing the resistance magnitude and response. Substrate materials were chosen based on materials that can be found in spacecraft or are typically used in engineering designs.

Table 2 – Substrate materials and CTE values

Substrate Material	CTE (ppm/°C)
1100 Aluminum	23.6
1018 Steel	11.5
Invar Alloy 36	1.5
Carbon Fiber	2.1

3.2 Specimen Fabrication

Samples were made using the steps in the following subsections. Each sample, regardless of substrate type, was made the same way. A few representative steps in this process can be found in Figure 10, which are explained in further detail later.

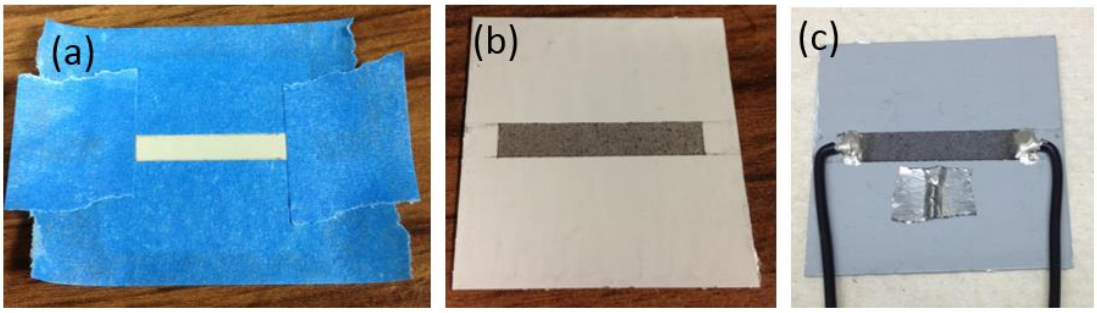

Figure 10 – (a) Sensor shape taped on substrate. (b) Tape removed after sensor application while the EG and latex was still damp. (c) Electrical connection applied to sensor with silver epoxy.

3.2.1 Substrate Preparation

A two-node sensor was made for calibration and twelve-sensor grids were made for thermal imaging. The substrate was cut into 40 mm and 75 mm squares for the two-node and twelve sensor grid samples, respectively. The substrate surface was sanded using 150 grit sandpaper (3M) to ensure primer adhesion. Two coats of the latex primer were applied manually to the substrate with a paintbrush until complete and even coverage was obtained. The first coat was allowed to dry for 5 minutes before the next was applied. The primer-coated substrates were allowed to dry for at least 24 hours in ambient conditions. Initial concerns about whether the sensor was attaching well to the substrate primer prompted us to sand the latex primer surface in order to roughen up the finish, allowing the sensor to adhere better to the substrate. Delaminating could produce false resistance responses, severely affect the results of the experiments. Tape (ScotchBlue) was used to make a stencil for the sensor shapes (Figure 10a).

3.2.2 Applying EG/latex Solution to Substrate

The composite EG and latex solution was spray coated (Badger, model 250-2), using an air pressure of 25 psi, over the stenciled area. Each layer was given approximately 5 minutes to dry before the next was sprayed. Spraying continued until the substrate was no longer visible, typically taking 8-10 layers. The tape stencil was removed (Figure 10b and Figure 11) while the EG and latex was still damp to avoid tearing the sensor. The samples were allowed to dry for at least 24 hours.

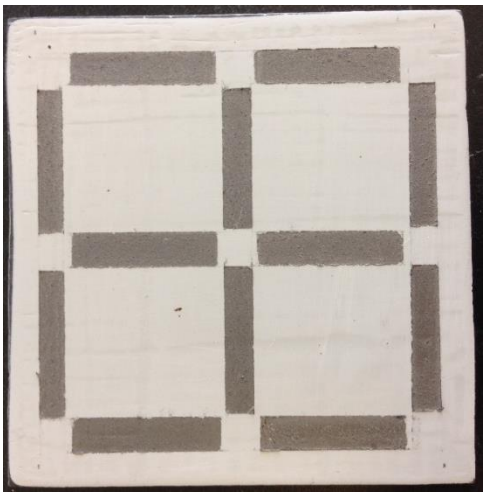

Figure 11 – Twelve sensor grid sample after tape mask was removed but before wires are connected.

3.2.3 Electrical Connections

Once the sensors were dry, conductive silver epoxy (CircuitWorks, CW2400) was used to attach stranded 24 gauge nickel-plated copper wire (NTE, WH24-00-100) at each node (Figure 10c). The wires were secured to the substrate with super glue (Loctite Super Glue Gel Control) to ensure that a tug on the wire would not affect the sensor connection. The epoxy was allowed to cure for at least 24 hours before the sensors were tested. Although the silver epoxy is conductive and does connect directly to the sensor, the interface resistance between the two materials is approximately 25

Ohms. This resistance was low compared to the sensor resistance and therefore has a negligible effect on the resistance reading.

3.2.4 Substrate-free Sensors

Although understanding how the sensors behave when applied to different substrate surfaces is important, it is also vital to understand how the sensor material behaves on its own without a substrate. Since the sensors have been sprayed directly onto the substrate until now, a new method was used. Casting the EG and latex solution is not plausible because the thickness cannot be kept uniform and the EG would separate from the latex and settle on the bottom during the drying process. To avoid these consequences, the substrate-free sensors were sprayed onto a glass substrate, allowed to dry, then were peeled off once the wires were attached.

Initially, the substrate-free sensors were sprayed onto the stenciled area of the glass. The sensors with a lower EG loading were able to be removed from the glass but underwent significant stretching. The higher EG loading sensors were unable to be removed because the EG percent was high enough to negate the elastomeric nature of the NR base polymer, making it brittle and not allowing for large deformations. Figure 12 shows how a 30% sensor failed when attempting to remove it from the glass.

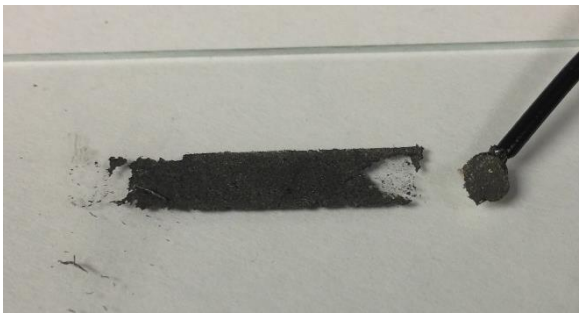

Figure 12 – Brittle 30% substrate-free sensor failure without latex base layer.

A layer of latex was sprayed on the glass before the sensor was applied to give the substrate-free sensor more stability without adding a CTE effect. This does not introduce additional substrate forces, makes the sensor thicker and less likely to break, and allows the sensor to be peeled off of the surface without too much deformation. The sensor being easily peeled off of the glass can be seen in Figure 13.

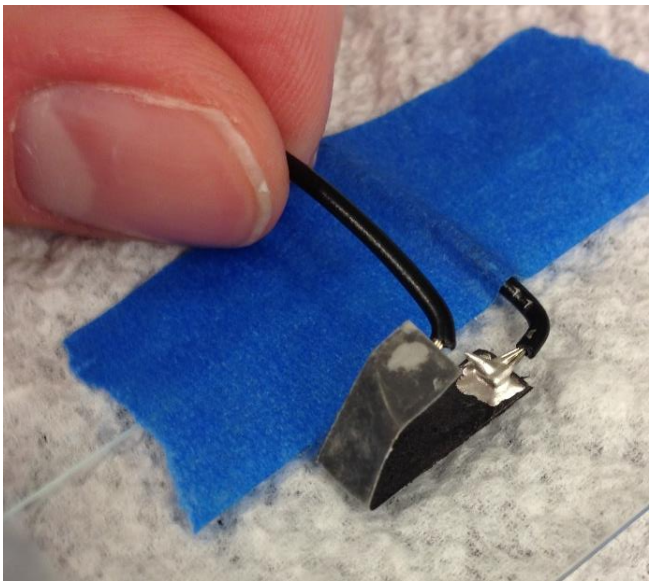

Figure 13 – Substrate-free sensor being easy removed due to thin latex base layer.

3.2.5 Thermal Conditioning

Once the sensor fabrication was completed, each sensor was thermally conditioned at 60 °C for one hour. This conditioning process was found to stabilize the sensor response, however the physics is not completely understood. The sensors are significantly affected by humidity [3], most likely because of the large free volume between the rubber polymer chains [39]. During the drying process, some water likely gets trapped between the polymer chains. The addition of thermal energy allows the polymer chains to move, thus expelling the remaining water molecules. If left in a humid environment, water molecules can get reabsorbed into the free volume between

the polymer chains, requiring additional conditioning. The humidity response reported previously for this material can be found in Figure 14.

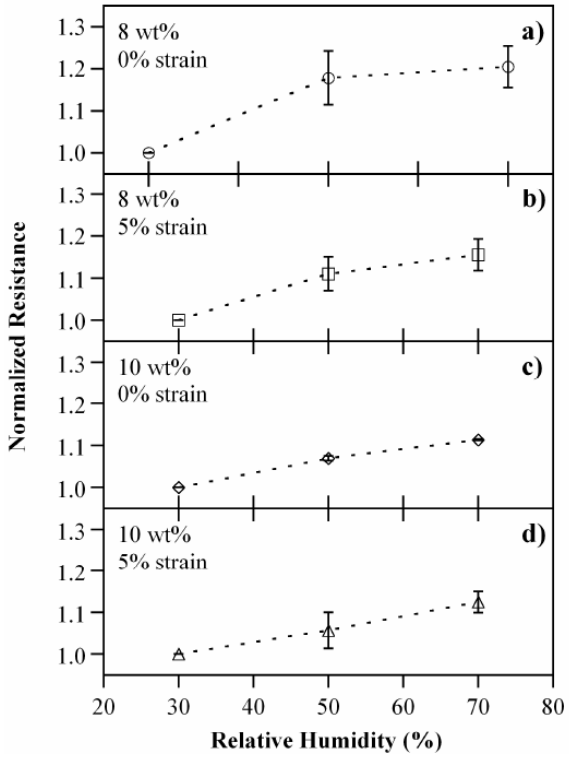

Figure 14 – Resistance response of EG and latex sensors to relative humidity [3].

3.3 Experimental Design

3.3.1 Data Acquisition

A data acquisition card (DAQ, National Instruments USB-6225) was used to collect the resistance and temperature data which was recorded by software (NI SignalExpress) at a 25 Hz sampling rate. Each analog resistance and temperature signal was passed through a 2 Hz low-pass filter (Butterworth) to reduce noise. The maximum thermal cycling frequency tested was 5 mHz, which is significantly lower than the filter cut-off frequency.

The analog inputs on the data acquisition card are able to read changes in voltage. In order to measure the resistance, the sensor(s) were placed in series with a 1 kΩ resistor and a constant voltage of 10 V was supplied (HP E3615A Power Supply) over the circuit. The voltage drop over each sensor and the resistor were recorded. The current was calculated using recorded the voltage drop over the 1 kΩ resistor. The known voltage drops over each sensor in the series and the calculated current allowed each sensor's resistance to be calculated for each time step.

Joule heating is when current flowing through a conductor creates heat and is dictated by the relationship in Equation 5. Joule heating was an initial concern because, depending on the equivalent resistance of the series, a constant voltage supply will output whatever current necessary to keep the voltage the same. If the current was too high, then the sensor would be heating up and experiencing much higher temperatures than intended during the experiment. The constant voltage was lowered to 1 V and the resistance was recorded, showing the same response as when 10 V was applied. This proved that Joule heating was not a concern.

Equation 5 – Joule heating energy relationship

$$Q \propto I^2 R$$

3.3.2 Test Set-up

The sensors were tested at both static and dynamic thermal loading conditions. These loading conditions were achieved by placing the substrates on a Peltier heater (model #8161, 40mm squared) which was powered by a bi-polar power supply (Kepco, BOP 20-10M). The voltage input to the heater was controlled by a function generator (Philips, PM5190 LF Synthesizer). To ensure a thermal contact between the heater and

the substrate, silicon thermal grease (RadioShack, Heat Sink Compound. 276-1372A) was used. The heater was also placed on an aluminum heat sink (Amico) so that during long experiments the temperature would not keep rising. A block diagram that depicts how the equipment is connected together can be found in Figure 15. The actual sensor test set-up for both the two-node and grid sensors can be found in Figure 16 and Figure 17, respectively.

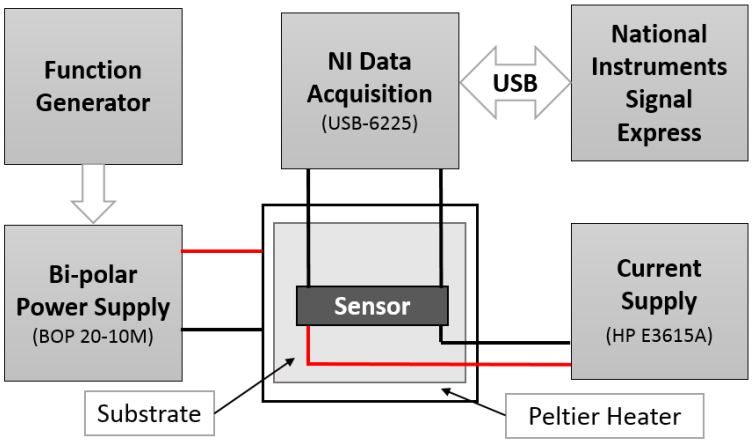

Figure 15 – Data acquisition block diagram used to collect the voltage drop over the sensor.

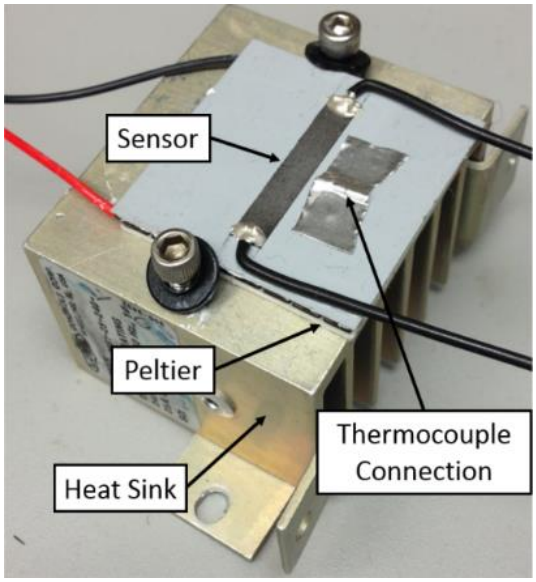

Figure 16 – Two-node sensor test set-up diagram.

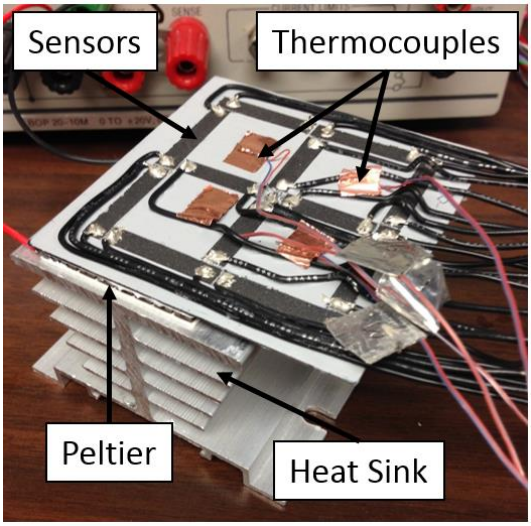

Figure 17 – Grid sensor test set-up diagram.

Thermocouples (T-type) were used to measure the temperature on the surface of the substrates to validate the temperature field simulations conducted later. One thermocouple was used for the two-node samples because of the uniform temperature and four were used on the twelve sensor grid samples.

3.3.3 Temperature vs. Resistance

In order to establish the temperature verses resistance calibration for the sensors, the resistance was recorded at various temperature steps. To accomplish this, the voltage step input to the Peltier heater ranged from 0 to 4 volts at 0.5 volt increments. Each step was held for approximately 5 minutes to allow the temperature response to plateau. The voltage input and corresponding temperature response can be found in Figure 18. The percent resistance change at each temperature step was recorded to determine the temperature and resistance response relationship above room temperature.

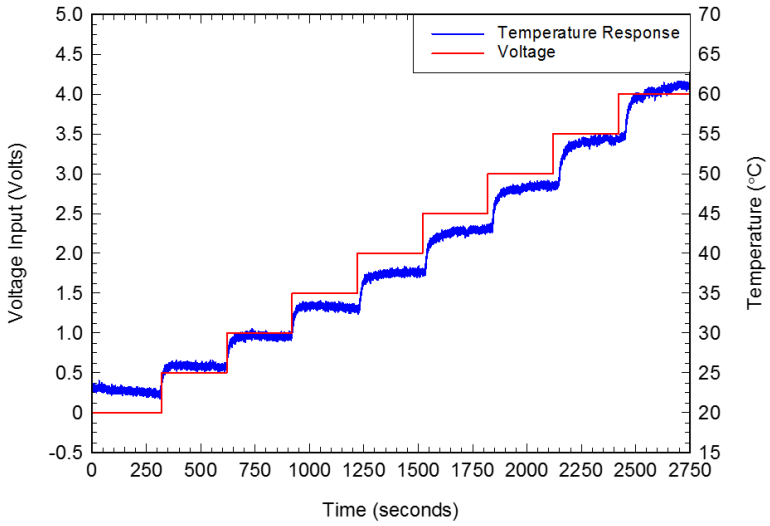

Figure 18 – Small voltage step function input and temperature response of Peltier heater.

The same experiment was conducted to determine the temperature and resistance relationship below room temperature. This experiment was conducted

similarly, however the voltage input range was 0 to -3 volts at 0.5 volt increments. The negative voltage input causes the temperature to decrease, giving the resistance calibration response below room temperature. The results from these experiments can be found in Chapter 4.

3.3.4 Step Function

The two-node sensor response was recorded for a step input. Ideally, the temperature input would be a perfect step function but the only way to control the temperature of the Peltier heater is the input voltage. The temperature measured on the surface of the substrate seen in the blue line in Figure 19 is affected by the time constant of the Peltier heater and the thermal conductivity of the substrate. The temperature exhibits a typical first-order response with a time constant of approximately 200 seconds. Figure 19 shows the voltage input and the temperature response of the Peltier heater during a step function experiment for the two-node sensors.

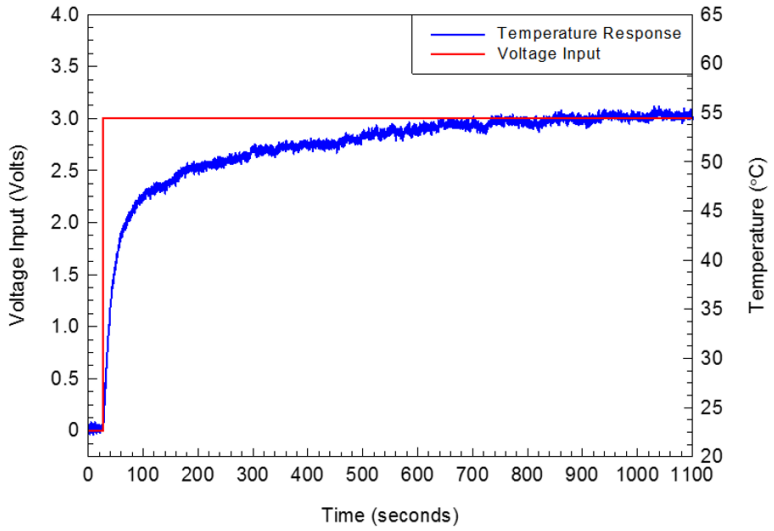

Figure 19 – Voltage step function input and temperature response of Peltier heater.

3.3.5 Sine Wave Function

Just as with the step function, the temperature during a sine wave experiment is controlled by the voltage input to the Peltier heater as prompted by the function generator. Figure 20 shows the exact 5 mHz voltage sine wave input and the typical temperature response of the Peltier heater as measured on the surface of the substrate by the thermocouples. It is clear that the temperature response is lagging due to the thermal conductivity of the substrate.

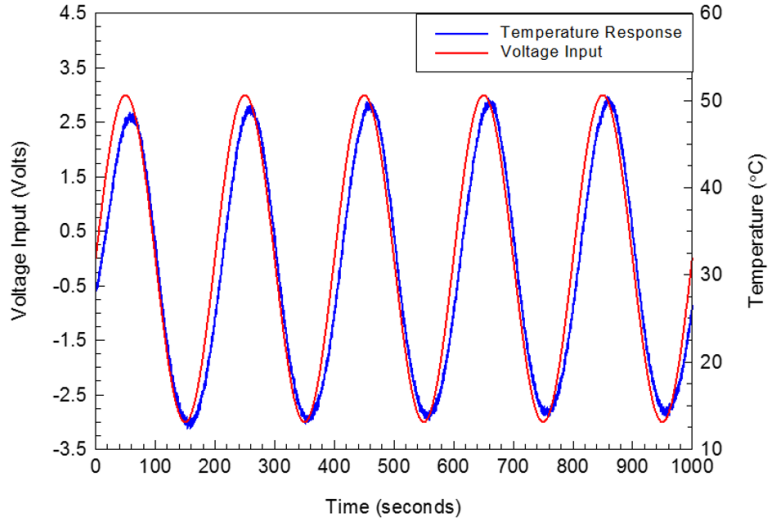

Figure 20 – Sine wave (5 mHz) voltage input and temperature response of Peltier heater.

3.3.6 Data Analysis

For all experiments described above, the resistances of the sensors are calculated based on the voltage drop measured by the DAQ. However, there was a large range in initial resistance for sensors that were made identically. It was not uncommon to observe resistances differing by an order of magnitude in some cases. This issue of reproducible resistances has not only been observed during this research, but also in other experiments [3,24]. To negate this issue, the resistance magnitude was normalized to show the percent resistance change, found in Equation 6.

Equation 6 – Percent resistance change calculation

$$\%\ \text{Resistance Change} = \frac{(R - R_0)}{R_0} * 100$$

Sensors made identically had similar percent resistance change response regardless of the initial resistance magnitude (R_0). The results presented in the next chapters will therefore show this normalized response.

Chapter 4 – Thermal Calibration of Sensing Material

In order to produce thermal images over a surface, the relationship between the resistance response of the sensors and the temperature input must be determined. Some variables that influence this relationship include the substrate on which the sensors are placed and the weight percent of EG in the sensors. The investigation of these factors as well as the calibration functions are presented in this section.

4.1 Substrate Comparison

The EG and latex composite was applied to four different substrates to observe the effect CTE had on the resistance response. The sensors were made with 25 wt% EG because during strain testing it was found that the EG and latex composite was elastomeric up until this loading level [10]. The resistance response to the 5 mHz temperature input for sensors on steel 1018, carbon fiber, aluminum 1100, and invar 36 can be found in Figure 21.

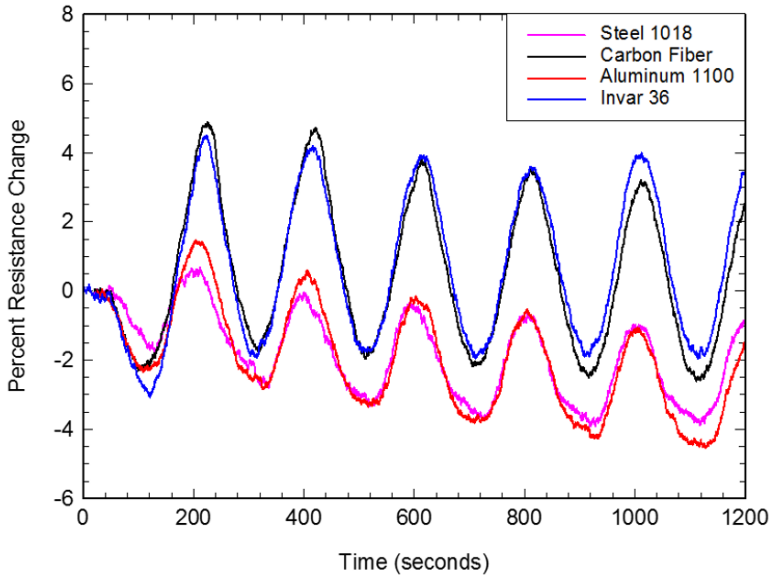

Figure 21 – Percent resistance response of 5 mHz temperature sine wave input for 25 wt% EG sensors on four different substrates.

This graph shows that there is not a correlation between the magnitude of percent resistance change and the CTE. If there were, the aluminum and invar substrate responses would be at opposite extremes with steel and carbon fiber between them. This is not the case according to Figure 21. What does depend on CTE is the overall transient decrease in the sinusoidal response over time. Invar, having a small CTE, shows almost no average decrease in percent resistance change over time while aluminum shows approximately a 1.5 % decrease over the 20 minute experiment. The sensor on steel has the second largest decrease over time, followed by the sensor on carbon fiber.

Despite this experiment, the carbon fiber substrate was chosen as the substrate for the calibration experiments. Since the motivation for developing these sensors is use in spacecraft, carbon fiber is most likely the substrate that the sensors will be applied to in practice.

4.2 Substrate-Free Sensors

To study the temperature and resistance relationship of the EG and latex composite material itself, without the influence of a substrate, substrate-free sensors were made. In order to observe the effect of EG loading on the substrate-free response, a 15 wt% EG and a 30 wt% EG sensor were made. The percent resistance change at each temperature step is plotted for each sensor along with the corresponding linear trend lines in Figure 22.

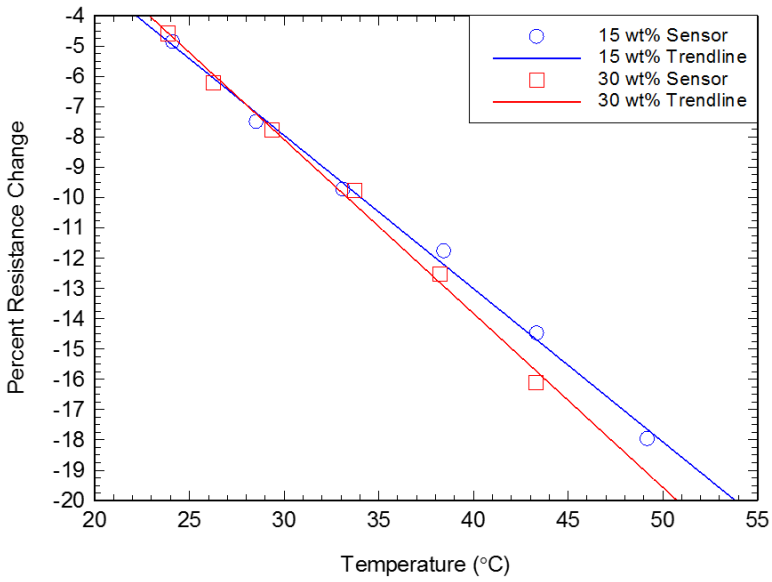

Figure 22 – Substrate-free sensor temperature vs. resistance relationship for 15 wt% and 30 wt% EG.

It is apparent that the EG loading level did not influence the temperature and resistance relationship for these substrate-free sensors. The trend lines for the 15 wt% and 30 wt% sensors reflect slopes of -0.506 $\frac{\%\Delta R}{T(°C)}$ and -0.574 $\frac{\%\Delta R}{T(°C)}$, respectively. The latex has a high CTE, and the lack of significant crosslinking in unvulcanized rubber means the latex matrix can expand much more than vulcanized rubber. The expansion of the material would likely cause the EG particle connections to decrease, causing an increase in resistance with temperature. However, the negative slopes found for both of these substrate-free sensors prove otherwise.

One explanation is that the sensor could have been unintentionally strained when securing the sensor into the test setup. This initial deformation would have increased the resistance. As temperature increased, the latex would have expanded, relieving the initial strain and therefore causing a decrease in resistance. These substrate-free sensors were unavoidably subjected to strain during handling. Although a resistance response was measured, the temperature and resistance relationship may

not accurately portray the temperature effects. However, the fact that there is no discernable difference between the EG loading levels shows the latex expansion dominates when there is no substrate.

4.3 EG Loading Effects

The next experiment investigates the effect of EG loading on the resistance response to temperature on a carbon fiber substrate. Initially, sensors containing 25 wt% EG were used because it was found to be an optimal loading level in regards to strain measurements because of the elastomeric behavior. Since deformations experienced due to temperature are a fraction of those experienced in strain measurements, elastomeric behavior was not as important. Therefore, sensors of 10 wt% through 30 wt% were tested. The initial resistances for each EG loading level sample can be found in Figure 23.

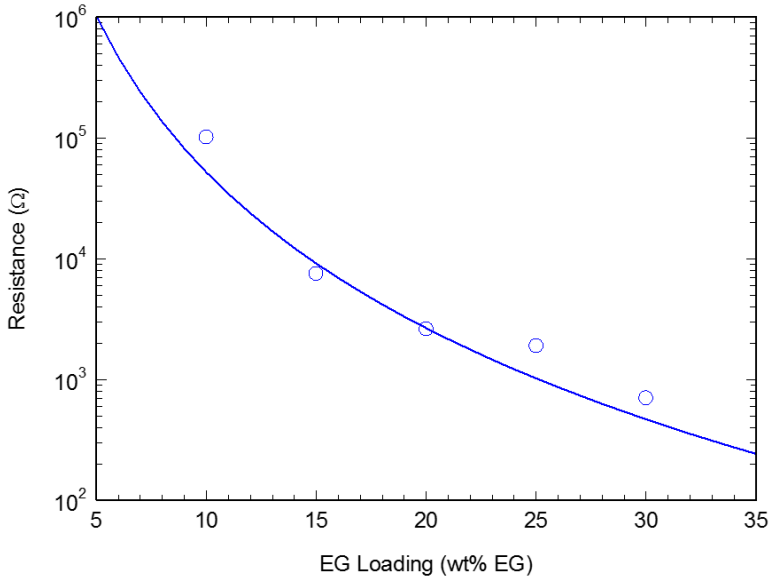

Figure 23 – Initial resistances at different EG loading levels to show percolation threshold effect.

This plot shows how resistance at room temperature changes when the concentration of EG is altered. This data follows the power law relationship expected

in a percolation model. Generally, percolation models describe the conductivity of a material $\left(\frac{1}{R}\right)$ and have positive exponents. Since resistance is being characterized, a negative exponent is expected. Figure 23 shows that the percolation threshold is between 5 wt% - 10 wt% EG.

The equation of the trend line in Figure 23, whose R^2 value is 0.959, can be found in Equation 7. The effect of the EG loading and resistance relationship is studied for the thermal step function and the 5 mHz sine wave experiments detailed in Section 3.3.

Equation 7 – Power law trend line for percolation experiment.

$$\text{Resistance} = 1e9 \cdot (\text{wt\% EG})^{-4.284}$$

4.3.1 Temperature vs. Resistance

The percent change in resistance for various EG loading levels was investigated as a function of temperature. The NTC linear relationship between resistance and temperature from the graphite and the power law relationship of the percolation effect will influence the sensors differently depending on the EG loading. The superposition of these two factors will produce the observed responses. The graphite effect will dominate with higher EG loading sensors, causing the temperature and resistance response to have an NTC linear behavior. At lower EG loading levels, the percolation effect will dominate, causing the response to follow a power law relationship. The superposition of these effects will be used to model the response. The percent resistance change was recorded for temperature steps above room temperature for each sensor and is presented in Figure 24.

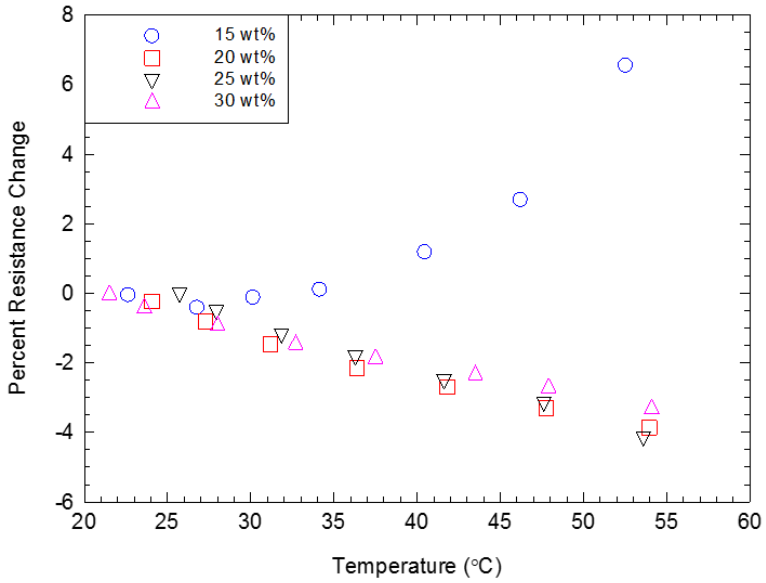

Figure 24 – EG loading effects on temperature vs. percent resistance change.

The 15 wt% sensor is the only one of the four that shows a positive percent change in resistance as temperature increased. The other three sensors show a similar negative linear response. However, the slope of the 20 wt% sensor begins to flatten out toward the higher temperatures. A model was made to fit this data as a function of temperature and EG loading.

The superposition of the linear and power law relationship effects that theoretically govern this behavior is shown in Equation 8. The first two terms represent the negative linear behavior of the graphite where V_{eg} is the percent EG, k_1 is a constant that depends on percent EG, and Ri is the resistance offset predicted at 0 °C. The second term is derived to match the power law relationship seen in the 15 wt% term where β is the power law exponent from the percolation theory and k_2 is a second constant that depends on percent EG. The values for the other variables from Equation 8 are presented in Table 3 for each sensor.

Equation 8 – Percolation and graphite effects on percent resistance change as a function of temperature

$$\%\Delta R = k_1(V_{eg}) \cdot T + R_i + k_2(V_{eg}) \cdot (T)^{\beta}$$

Table 3 – Constants for temperature and resistance as a function of EG loading model

EG %	k_1	k_2	Ri
15	-0.113	4.0e-7	2.5
20	-0.160	5.0e-8	3.5
25	-0.140	5.0e-9	3.5
30	-0.095	1.0e-9	1.7

The most influenced constants by EG loading is k_2 because that is the term that established how much of the power law relationship is prevalent. The k_1 constant dictates the slope of the linear portion which changes between samples. In order to make the model work for any EG loading level, k_2 was calculated as a function of EG loading. Given the four data points calculated from this data, the best fit was found and is presented in Equation 9.

Equation 9 – Percent EG influence on constant, k_2, for temperature and resistance model

$$k_2 = 0.0002e^{-0.406 \cdot (\%EG)}$$

The constant k_1 was between -0.160 and -0.095 for the four sensors, however an EG relation could not be made. Instead, the relationship can be described as a function of the initial sensor resistance, R_0. Graphite typically has a temperature coefficient, α, of -0.00045 $\frac{\Omega}{^{\circ}C}$. If R_0 of the sensor at room temperature is around 290 Ω, then this temperature coefficient would make k_1 approximately -0.130 $\frac{\%\Delta R}{^{\circ}C}$ which is the average of the experimental data found. This R_0 value is a typical initial resistance found in sensors, proving this is a reasonable analysis. Equation 10 shows the final model equation for this data. The graphical display of this model for the data can be found in Figure 25.

Equation 10 – Percent resistance model as a function of temperature and percent EG

$$\%\Delta R = \frac{\alpha_{graphite}}{R_0} \cdot T + R_i + 0.0002 \cdot e^{-0.406 \cdot (V_{eg})} \cdot T^{\beta}$$

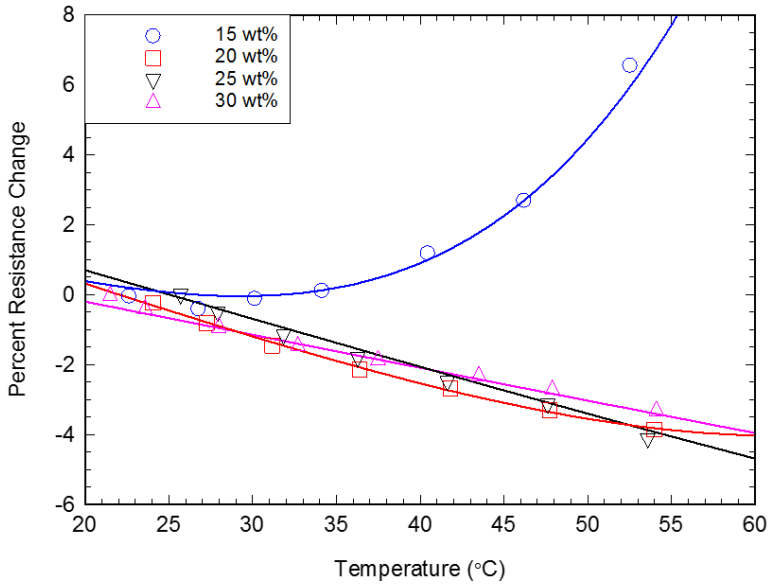

Figure 25 – Temperature and resistance as a function of EG loading with best fits from model.

The analysis of the temperature and percent resistance change effects of this material as a function of EG loading will benefit characterization of this material in future experiments. This research ultimately focused on calibrating one EG loading level so this model was not used to predict temperature fields.

4.3.2 Step Function

The different EG loading sensor responses to the step function are shown in Figure 26. Figure 26 (a) shows the resistance response from all EG loading sensors whereas Figure 26 (b) omits the 10 wt% sensor.

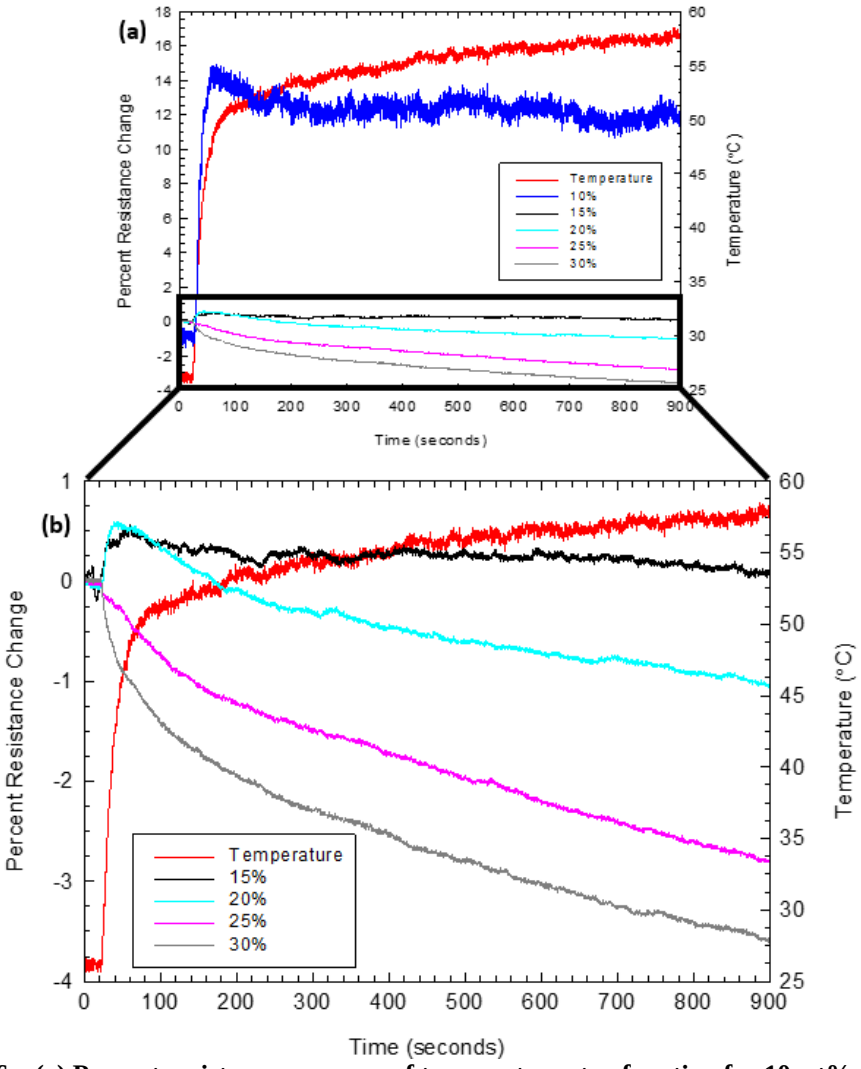

Figure 26 – (a) Percent resistance response of temperature step function for 10 wt% - 30 wt% EG sensors. (b) Plot without 10 wt% sensor.

It is clear that the 10 wt% sensor has a different response to the temperature step function. This difference in behavior is likely because the 10 wt% sensor is close to the calculated percolation threshold of 7.5 wt% EG shown in Figure 23. Figure 26 (b) shows that as the loading level increases, the more stable the resistance response is. Visually, it is clear that the response of the lower loading level sensors stabilize faster over time. Ideally a faster time constant is desired, however the 30 wt% sensor shows the most consistent response and does not have an initial resistance increase like the 15 wt% and 20 wt%.

4.3.3 Sine Wave

The same four sensors were exposed to the 5 mHz temperature sine function. The resistance response for each EG loading level can be found in Figure 27.

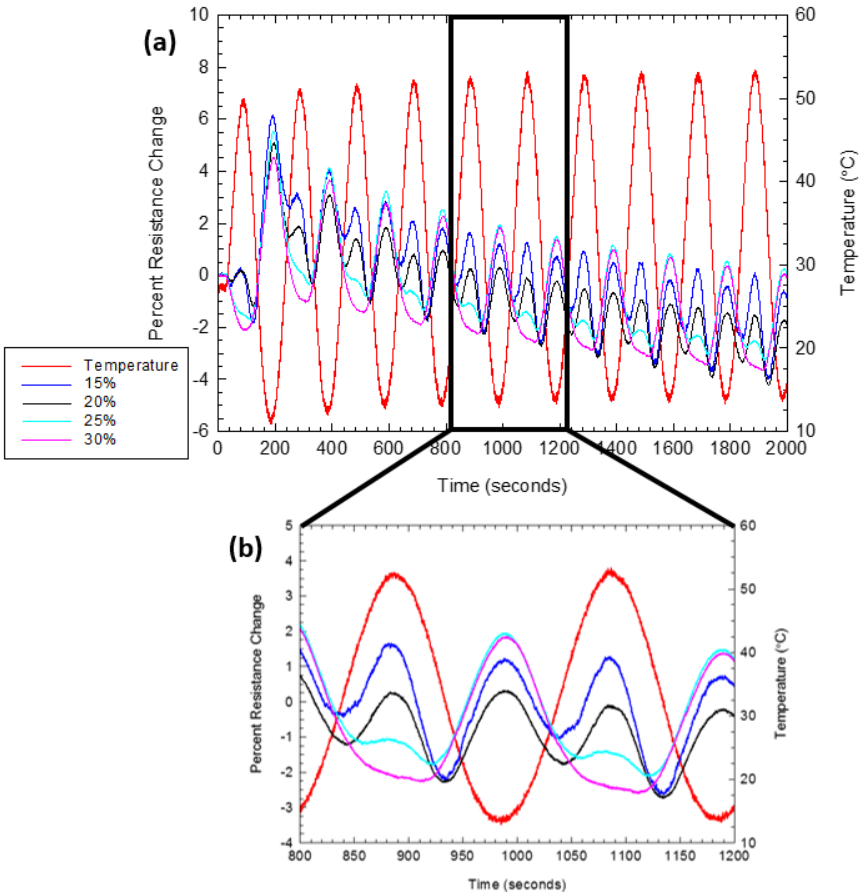

Figure 27 – (a) Percent resistance response of 5 mHz temperature sine wave input for different EG loadings. (b) Closer look at resistance response to show "double hump".

One noticeable trend is the transient decrease in average resistance over time. This can be attributed to the CTE effect of the carbon fiber substrate, discussed previously. Figure 27 (b) shows a more detailed view of the responses. Some of the lower EG loading sensors have a second peak, otherwise referred to as a "double hump". However, as the weight percent of EG increases to 30 wt%, the magnitude of the second peak vanishes.

The second peak in resistance, corresponding to the highest temperature, is likely caused by thermal expansion. This explains why it only occurs in lower EG loading because there is more latex matrix to expand. As the number of EG particles increases, the material begins to act more like graphite. As discussed in Section 2.7, graphite's conductivity decreases with temperature. The decrease in magnitude of the peak as EG loading increases shows the opposing resistance effects of the thermal expansion and the graphite material behavior. The lack of a second peak in the 30 wt% sensor shows that this is the point where the graphite effect dominates the bulk material response.

A model was derived to fit the data presented in Figure 27 and to predict the affect EG loading has on the "double hump". The general form of this model, in Equation 11, shows three governing functions. The first is a sine wave response with the same frequency as the temperature input because of the linear relationship of the graphite. The second function is the harmonic to the first, providing the "double hump" pattern. The final function reflects the transient decrease in resistance over time in the form of an exponential relationship.

Equation 11 – Time dependent percent resistance change model as a function of EG loading

$$\%\Delta R = A \cdot \sin(0.01\pi t) + B \cdot \sin(0.02\pi t + \varphi) + C \cdot e^{Dt} + E$$

Table 4 – Constants for time-dependent percent resistance change model

% EG	A	B	C	D	E	φ
15	0.15	-1.3	11	-0.00035	-8	0.55π
20	-0.10	-1.0	10	-0.0005	-7	0.60π
25	-1.70	-0.7	8	-0.00036	-6	0.55π
30	-2.00	-0.5	6	-0.001	-3.25	0.55π

The constants that show a dependence on EG loading are A, B, C, and E. As the EG loading increases, the constant A decreases but B increases, creating the "double

hump" response. The constant C decreases with an increase in EG loading because it affects the magnitude of the sine wave, mimicking the decrease in magnitude with EG loading observed in the experimental data.

4.4 30 wt% EG Sensor on Carbon Fiber

Since the 30 wt% sensor showed the expected step function response and had a single peak resistance response to the sine wave function, 30 wt% was chosen as the EG loading to move forward within the calibration process. This section will present how the temperature and resistance calibration experiments were conducted.

4.4.1 Temperature vs. Resistance Calibration (Room Temperature and Above)

To find the relationship between the temperature and resistance response of the 30 wt% sensors, resistances were measured at various temperature steps from room temperature (RT) and above. Five identical samples were tested and the fitted data is presented below. Table 5 presents the slope and intercept values from the linear trend lines.

Table 5 – Linear best fit parameters for each 30% two-node calibration samples

	Sample 49	Sample 50	Sample 51	Sample 52	Sample 53	Average
Slope	-0.088	-0.080	-0.097	-0.075	-0.062	-0.080
Intercept	1.718	1.553	1.874	1.103	1.008	1.451
R^2	0.985	0.973	0.991	0.968	0.944	N/A

The data points and linear best fit curves are presented in Figure 28 and the average fitted curve can be found in Figure 29. One standard error above and below the averaged curve was calculated and is shown in Figure 29 with dashed lines.

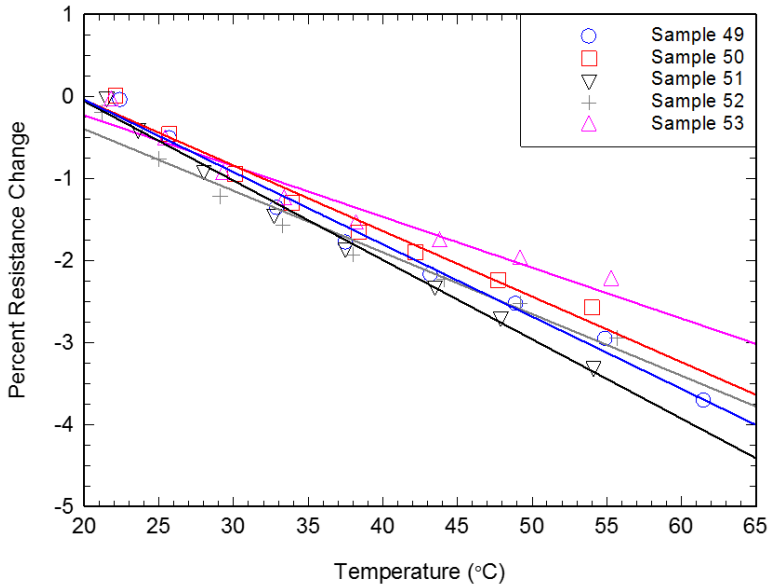

Figure 28 – Temperature vs. resistance scatter plot and best fit lines of 30 wt% two-node calibration sensors for room temperature and above.

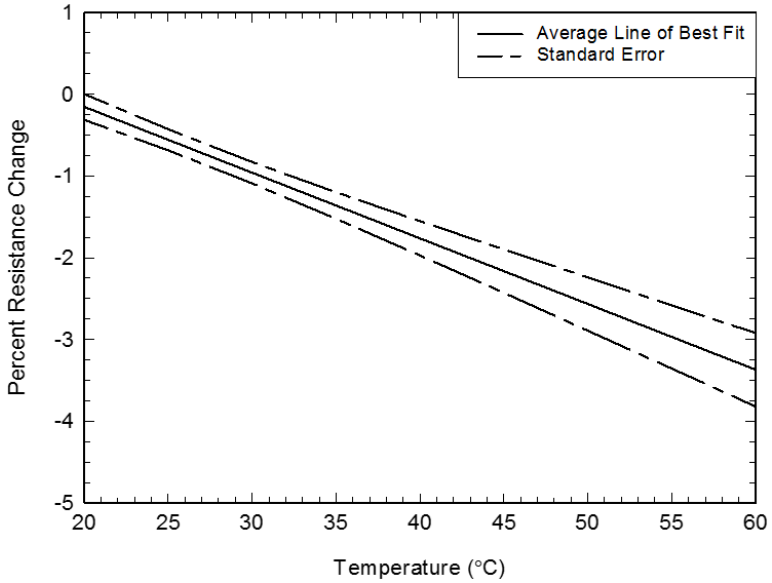

Figure 29 – Temperature vs. resistance average best fit line and standard error brackets for room temperature and above.

The responses in Figure 28 show that as temperature increases, percent resistance change for each sensor begins to deviate from one another. Despite this, each sensor shows the same negative linear correlation. The standard error brackets in Figure 29 show that 68.2% of all data taken should fall within the dashed lines. The averaged best fit line for this data set will be used as the calibration function later and

can be found in Equation 12. This function will allow resistance data that is collected above room temperature to be converted into temperature in °C.

Equation 12 – Calibration equation for temperature vs. resistance of 30% sensor on CF (room temperature and above)

$$\text{Percent Resistance} = -0.080 * \text{Temperature} + 1.451$$

4.4.2 Temperature vs. Resistance (Room Temperature and Below)

The same experiment was run except this time the voltage input to the Peltier heater was inverted, exposing the sensors to temperatures below room temperature. The behavior below room temperature showed an exponential trend, whose form can be found in Equation 13. The constants A and c for each experiment can be found in Table 6. The difference between the average constant, c, and the value for each sample is labeled "Delta".

Equation 13 – Exponential equation form

$$y = Ae^{cx}$$

Table 6 – Exponential fit parameters for each 30% two-node calibration samples

	Sample 49	Sample 50	Sample 51	Sample 52	Sample 53	Average
A	2.140e5	1.651e5	9.524e4	2.562e5	1.353e4	1.488e5
c	-0.782	-0.746	-0.739	-0.800	-0.562	-0.726
Delta	0.056	0.020	0.013	0.074	0.164	N/A
R^2	0.999	0.992	0.998	0.996	0.992	N/A

An outlier analysis was conducted on the data sets because the constant, c, for Sample 53 was noticeably lower than the rest. A modified Thompson tau test was conducted to check if there are any outliers. For a sample size of 5, the modified Thompson constant, τ, is 1.571. The standard deviation of the constants, c, for all five samples is 0.095 and therefore the product of τ and the standard deviation is 0.149. According to the modified Thompson tau test, if the value of delta is greater than the

product of τ and the standard deviation, then the data point is considered an outlier. This means that Sample 53 is in fact an outlier.

The data points and trend lines for Samples 49-52 can be found in Figure 30. The averaged trend line and standard error for the data set can be found in Figure 31. It should be noted that any data points below 10 °C were omitted from this analysis because condensation began forming at this temperature and the resistance response stopped changing.

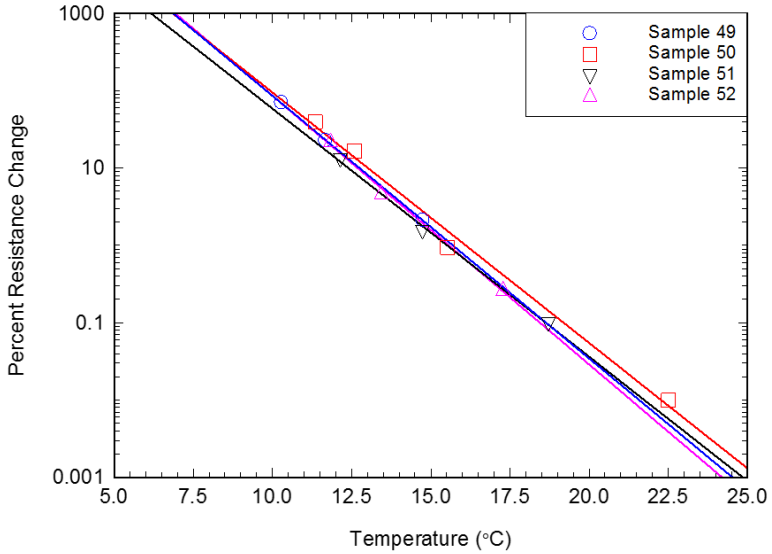

Figure 30 – Temperature vs. resistance scatter plot and best fit lines of 30 wt% two-node calibration sensors for room temperature and below.

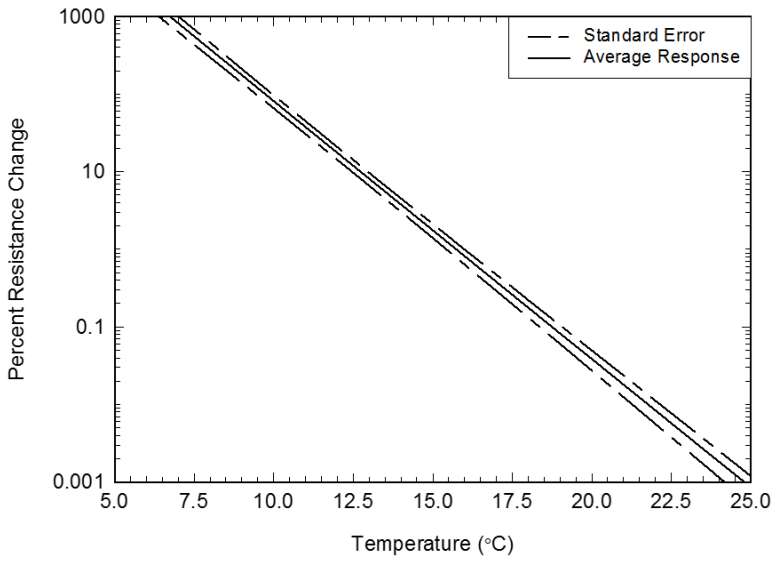

Figure 31 – Temperature vs. resistance average best fit line and standard error brackets for room temperature and below.

The average temperature and resistance calibration function is calculated based on the average of the remaining four samples. This function can be found in Equation 14 and will be used to calculate temperature from resistance data that is collected below room temperature.

Equation 14 – Calibration equation for temperature vs. resistance of 30% sensor on CF (room temperature and below)

$$\text{Percent Resistance} = 1.826\text{E}5 * e^{-0.767 * \text{Temperature}}$$

4.4.3 Step Function

The same five 30 wt% EG sensors were exposed to the temperature step function to understand the resistance response over time. Figure 32 shows the percent change in resistance of the five samples and the temperature input. The experiment was run for approximately 30 minutes to allow the resistance response to stabilize.

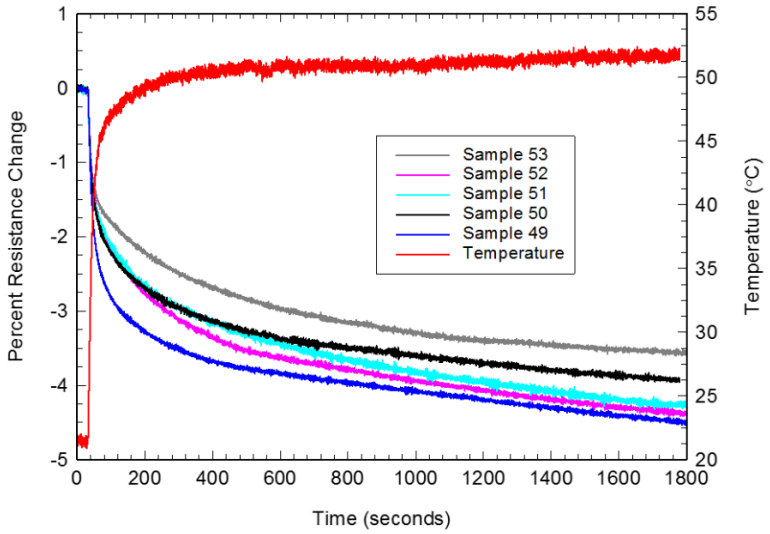

Figure 32 – Percent resistance response of temperature step function for 30 wt% sensor on carbon fiber substrate.

Each of the five samples was made identically and at the same time. Despite this, there is some deviation between the percent resistance changes over the 30 minute experiment. However, the maximum difference between responses is approximately 1%. The average response from this data set as well as the standard error can be found in Figure 33. This data offers insight to the time required for these sensors to fully respond to a temperature input.

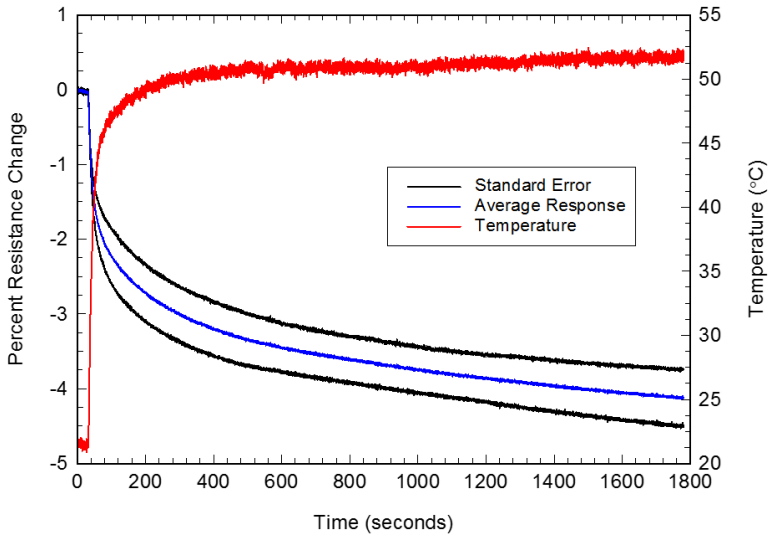

Figure 33 – Average response and standard error from two-node step function experiment.

4.4.4 Sine Wave

The sensors were exposed to the sine wave input and the resistance responses for each sample can be found in Figure 34.

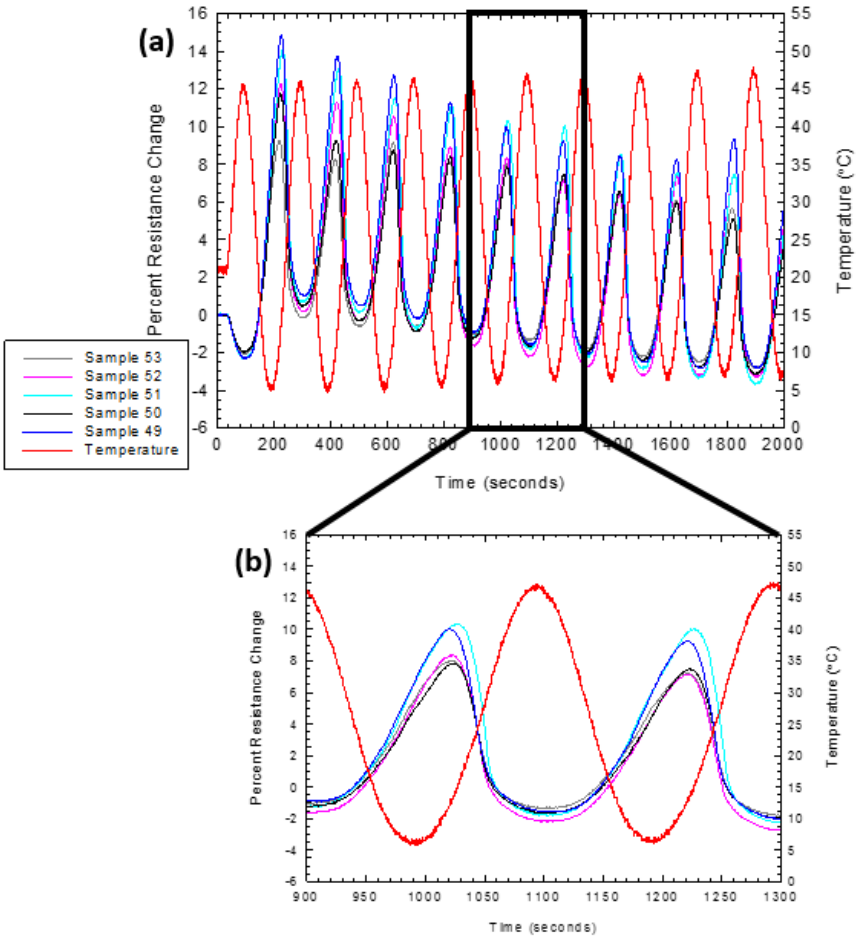

Figure 34 – (a) Percent resistance response of 5 mHz temperature sine wave of five identical 30 wt% sensors on carbon fiber substrate. (b) Zoomed in to observe details in response.

The five sensors behave relatively the same as noticed in the closer look provided in Figure 34 (b). The magnitudes vary slightly but all fall within the same standard error. The average sine response with standard error brackets for this experiment is shown in Figure 35.

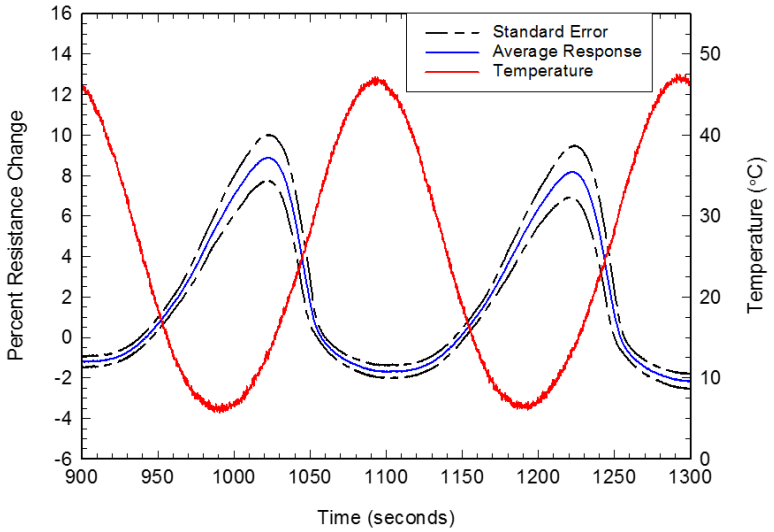

Figure 35 – Average resistance response and standard error for two-node sine wave experiment.

Figure 35 shows that at temperatures below room temperature, the resistance response lags more, as evident in off-centered resistance peaks. The sensors also had a faster response when the temperature increased than when it decreased. In terms of the error, the standard deviation between the five samples was consistently larger at the lower temperatures than at the higher ones. This means the sensors will respond more predictably at temperatures above ambient conditions than below.

4.5 Calibration Conclusions

The EG and latex composite sensors were thermally characterized and the effects of substrate CTE and EG loading level were investigated. Percolation theory was used to determine the resistance and loading level relationship. This power law function was used to create the model for the temperature verses percent resistance change as a function of EG loading. It also helped understand the EG loading effect on the step and sine input functions. The EG loading effect on the sine wave input was also modeled to show the three parent functions involved in the signal. There is a linear

graphite response, a harmonic “double hump” response, and an exponential decay transient effect. Constants for all sensor types were presented.

The 30 wt% sensor on carbon fiber was calibrated because it exhibited the most stable and predictable response. Five identical sensors were made and averaged to produce calibration functions above and below room temperature. The standard errors show how repeatable the responses should be for both input functions. These models and the statistical analysis characterize the material enough to predict the temperatures corresponding to a given resistance reading. Calibration functions developed in this chapter will be used in the next to convert the resistances into temperatures.

Chapter 5 – Twelve Sensor Grid Results and Discussion

Twelve sensors were sprayed onto a larger carbon fiber substrate in a 9-node grid pattern. The resistance from each sensor should reflect the temperature distribution of the substrate. Using the calibration functions established in the previous chapter, these resistances can be converted into temperatures. Thermal images can be produced by creating contour plots by correlating the calculated temperatures to the sensor location in the grid. These grid sensors were tested under two different temperature distributions both above and below ambient conditions. Each of the twelve sensor grid experiments are discussed in this chapter.

5.1 Thermal Simulations

Although temperature contour plots can be generated by the resistances from the grid sensors, simulations were conducted to have a theoretical thermal image to compare the experimental data. The specifics of these thermal simulations are detailed in this section.

5.1.1 Simulation Set-up

Finite element analysis (FEA) simulations using Creo Parametric 2.0 were conducted to produce the theoretical temperature distributions over the substrate surface. Unlike the two-node sensors, the larger grid sensors undergo a non-uniform temperature distribution. A solid model of the plate, measuring 75mm square with a thickness of 0.8 mm, was used for the simulations. The bottom surface was split to reflect the size and placement of the Peltier heater. A custom material was made in the program to mimic the carbon fiber substrate as closely as possible. The material

properties of the carbon fiber as well as the properties of the ambient air can be found in Table 7.

Table 7 – Material Properties and Parameters for Thermal Simulation

Carbon Fiber Material Property	**Values**
Density, ρ	$1.76\ \frac{g}{cm^3}$
Poisson's Ratio, ν	0.3
Young's Modulus, E	228 GPa
CTE, α	$2.1\ \frac{ppm}{°C}$
Thermal Conductivity, k	$0.4\ \frac{W}{m \cdot K}$
Ambient Air Properties	**Values**
Bulk Air Temperature	22 °C
Heat Transfer Coefficient of Air, h	$0.95\text{-}0.80\ \frac{W}{m^2 \cdot K}$

Since the material properties of woven carbon fiber composite can vary greatly, the chosen values were based on similar materials and varied until the profiles reflected the temperatures measured with the thermocouples during the experiments.

5.1.2 Simulation Results

The properties in Table 7 were used to define the carbon fiber material in the thermal simulation. A heat load of 125-150 mW was applied to the split bottom surface. This split surface was defined as a 40 mm square directly in the middle of the substrate or in the upper left corner of the substrate for the centered heater and corner heater experiments. Every other surface had a convection condition applied to simulate the free convection of the air around the sample. These conditions can be seen in the screen shot from the centered heater simulation, found in Figure 36.

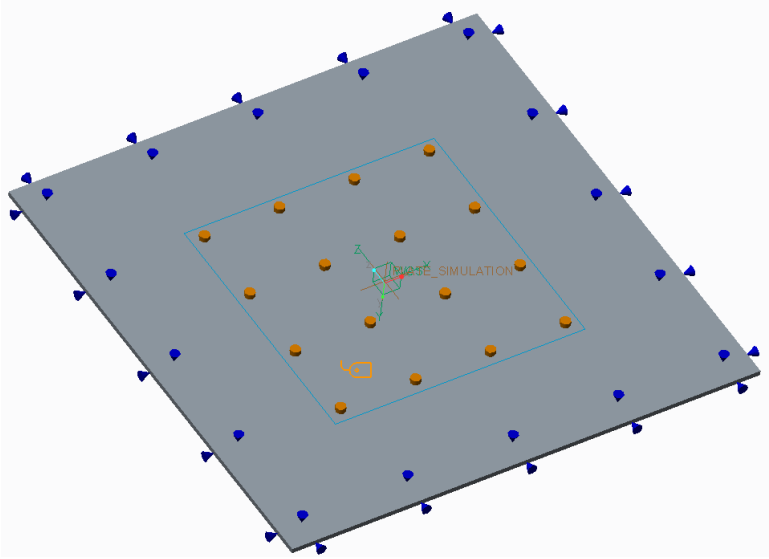

Figure 36 – Plate model in Creo Parametric with heat load (yellow), convection boundary condition (blue), and split surface (blue square).

Two fundamental heat transfer methods are used to calculate the temperature fields in the simulations. Conduction is the mechanism responsible for how the heat is transferred between the heater and substrate by means of thermal grease and how that energy is carried through the solid carbon fiber material. Conduction is governed by Equation 15 where Q is heat in Joules, k is the thermal conductivity of the material in $\frac{W}{mK}$, A is the surface area in contact with the heat source in m^2, and T is the temperature in Kelvin.

Equation 15 – Conduction governing equation.

$$\frac{dQ}{dt} = -kA\frac{dT}{dx}$$

The second fundamental heat transfer method is convection. This is when heat is added or removed from a system due to the flow of air or fluid on a surface. Since these experiments were not conducted in a vacuum, free convection of air was included as a boundary condition. The governing equation of convection in Equation 16 depends

additionally on the heat transfer coefficient of the moving fluid in $\frac{W}{m^2K}$ and the surface and ambient temperatures, both measured in Kelvin.

Equation 16 – Convection governing equation.

$$\frac{dQ}{dt} = hA(T_{surface} - T_{ambient})$$

The FEA algorithm uses the heat input on the bottom surface and the convection condition as the boundary conditions for the problem while the material properties dictate the actual temperature distribution of the material. The lower the thermal conductivity of the material, for example, the steeper the temperature gradient produced. The results of the centered heater temperature distribution can be found in Figure 37 and the corner heater temperature distribution can be found in Figure 38.

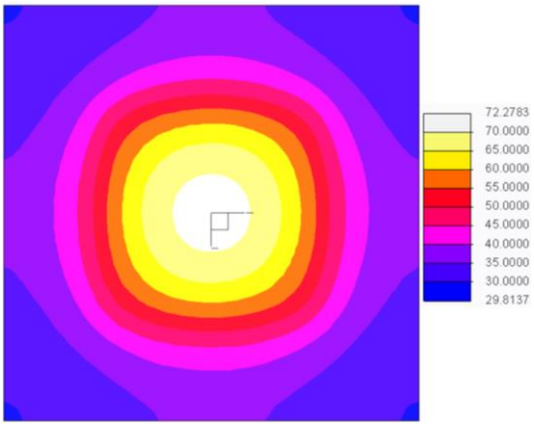

Figure 37 – Temperature (°C) distribution simulation of a centered heater on the grid samples above room temperature.

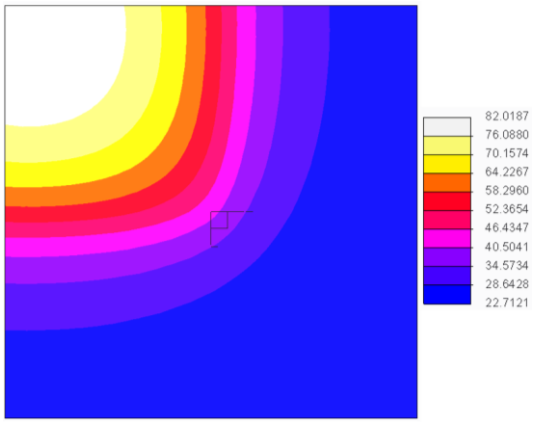

Figure 38 – Temperature (°C) distribution simulation of a corner heater on the grid samples above room temperature.

Comparing the two temperature distributions, it is apparent from the temperature scales on the right of the figures that the corner heater creates a larger temperature gradient and has a higher maximum temperature. It is also important to note that the symmetries of each temperature distribution will impact the resistance distribution for each experiment.

The same simulations were run again, however this time the heat load was negative to simulate heat leaving the system. The temperature distribution for the centered heater below room temperature and the corner heater below room temperature are shown in Figure 39 and Figure 40, respectively.

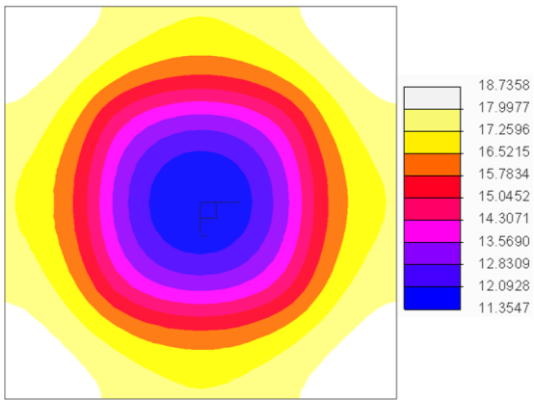

Figure 39 – Temperature (°C) distribution simulation of a centered heater on the grid samples above room temperature.

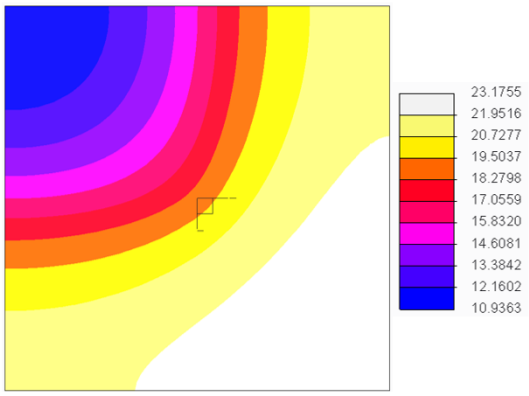

Figure 40 – Temperature (°C) distribution simulation of a corner heater on the grid samples below room temperature.

5.2 Centered Heater Results

The first experiment conducted with the twelve sensor grid samples was one with a heat source placed in the center of the sample. The placement of the Peltier heater, the location of the twelve sensors, and the location of the four thermocouples can be found in Figure 41.

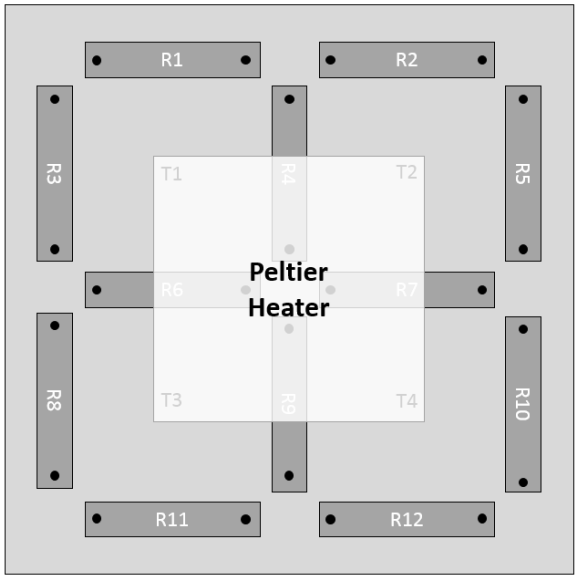

Figure 41 – Peltier heater placement and sensor diagram for centered heater experiment.

There were five twelve sensor grid samples that were made and tested under identical conditions. The data for each sensor from all five samples were averaged to produce the results presented below for the step and sine wave experiments.

5.2.1 Step Function Response

The resistance field measured by the twelve sensor grid should mimic the temperature field seen in the centered heater thermal simulation (Figure 37). The sensors labeled R4, R6, R7, and R9 should have the largest decrease in percent resistance change according to the results of the two-node sensor experiments. Theoretically, these four sensors should have the same exact resistance response. Some assumptions made are that the heater was perfectly centered, the heat load was uniform, and the sensors were identical. The eight remaining sensors should have a lower magnitude change than the center sensors but should still show a negative percent change in resistance. The experimental results of the temperature step function with the centered heat load can be found in Figure 42.

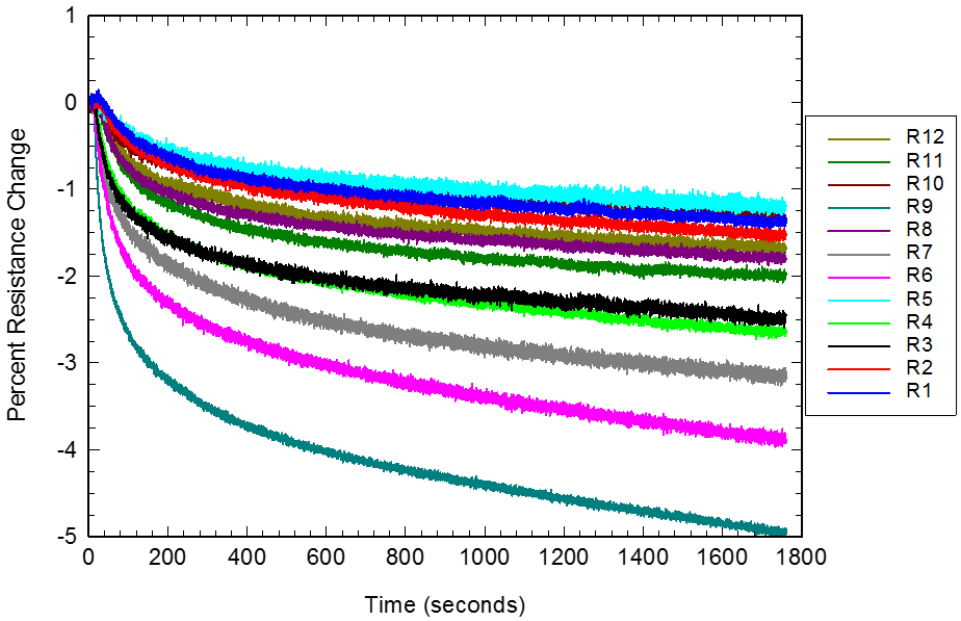

Figure 42 – Sensor grid resistance response to a temperature step function with a centered heater.

Theoretically, Figure 42 should show one step response for R4, R6, R7, and R9 and another for the other eight. However, the experimental data shows a range of resistance responses. This can be explained due to imperfections in the test setup such as a misaligned heater or in the composition of the sensors such as the thickness or EG particle orientation. Figure 42 does show that the center sensors have a larger change in magnitude, whereas the surrounding sensors have a smaller decrease in resistance. As predicted by the two-node calibration experiments, all sensors have a negative percent change in resistance. The responses of the four centered sensors and the eight surrounding sensors are displayed separately in Figure 43 and Figure 44.

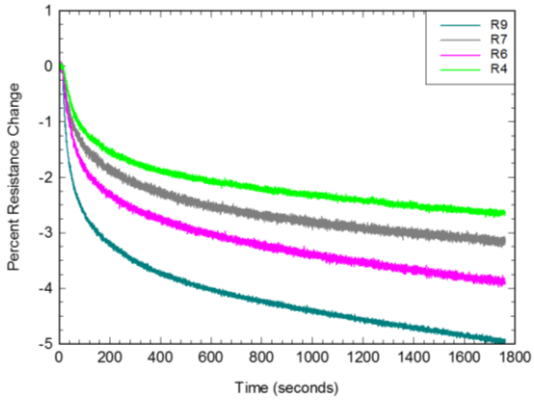

Figure 43 – Most responsive sensors to centered heater step function.

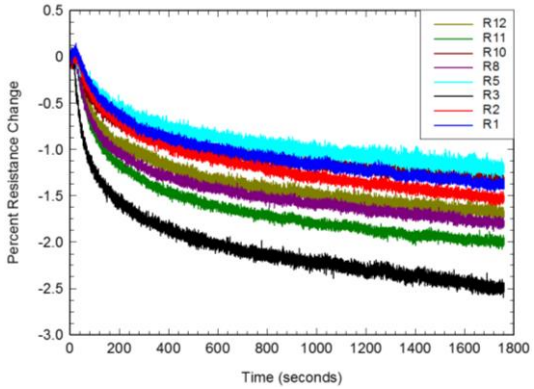

Figure 44 – Least responsive sensors to centered heater step function.

It is evident in Figure 43 that the resistance of R9 and R6 decreased the most, correlating to a higher temperature. This likely indicates that the Peltier heater was slightly southwest of center. Figure 42 shows that the R3 sensor response is approximately equal to the R4 response. This would, again, indicate a non-symmetric temperature field. The eight outside sensor responses are more grouped together than the four centered sensors and have a smaller percent resistance change response, as expected. Although the sensors show a slightly non-uniform field, the general response that was expected is reflected in this experiment.

This data was imported into a MatLab function to create a contour plot of the resistance field over the substrate's surface. This script places the resistance values from each sensor in the middle of the sensor's location and averages the resistances of adjacent sensors at the intersections to give the plots more resolution. This MatLab script can be found in Appendix A. The resistance field produced from the center heater can be found in Figure 45.

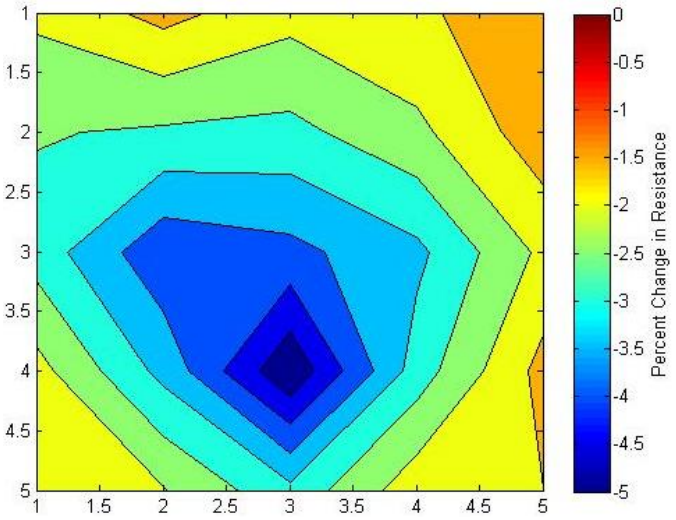

Figure 45 – Final resistance response from centered heater step function experiment.

The resistance data was taken from the last time step in the step funciton experiment to show the largest change in percent resistance. The resistance field should be symmetric about the center, however it is clearly skewed slightly lower. The heater was likely a tad off center, causing the shift.

5.2.2 Sine Function Response

The grid sample was tested with the sine wave input while the heater was near the center. Again, the four centered sensors are expected to respond the most while the eight surrounding sensors should be less responsive as the calibration experiments predict. Figure 46 shows the twelve sensor responses to the same temperature input presented earlier in Figure 20.

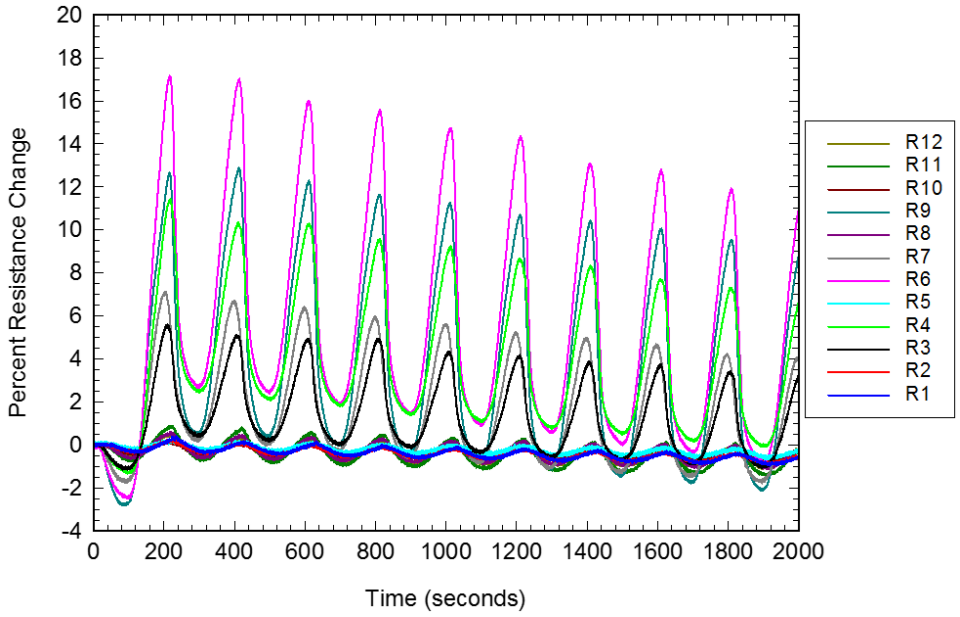

Figure 46 – Sensor grid response to a centered heater 5 mHz sine wave thermal load.

The center sensors (R4, R6, R7, and R9) have the highest percent resistance change magnitude, however R6 and R9 have the largest response. It is apparent that R3 also has a prominent response compared to the other outer sensors. A closer look at the center sensors and R3 (Figure 47) and the surrounding sensors (Figure 48) are presented.

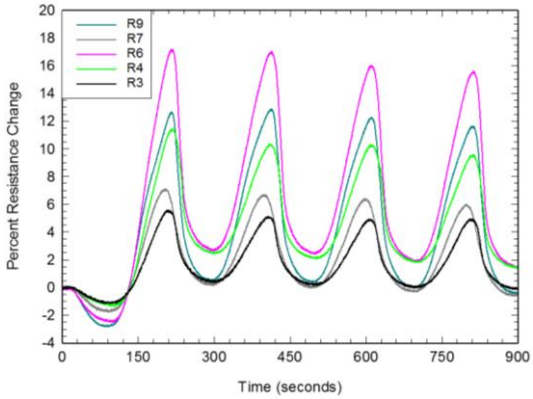

Figure 47 – Most responsive sensors to centered heater 5 mHz sine wave function.

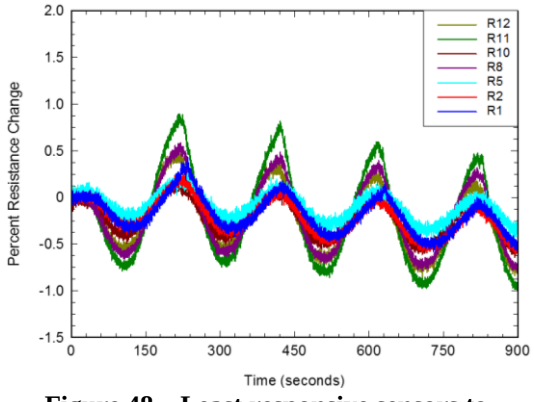

Figure 48 – Least responsive sensors to centered heater 5 mHz sine wave function.

One important trend to note is that when the sensors are more responsive, the first peak is well above the initial room temperature resistance. Over time the average

resistance response decreases but for the most part, the peaks and valleys remain above the initial resistance. In contrast, the least responsive sensors seen in Figure 48 tend to have a sine function that averages around the initial room temperature resistance reading. The outside sensors also show a decrease over time but the response is not as prominent as the transient response of the center sensors.

The resistance data from the sine wave experiment was imported into the same Matlab function to produce a contour plot of percent change in resistance over the surface of the substrate. Since the resistance from a high temperature experiment was already presented in the step function contour plot, the first temperature valley in the sine wave experiment was chosen to present. Figure 49 shows the data from the first temperature valley, otherwise known as the first resistance peak.

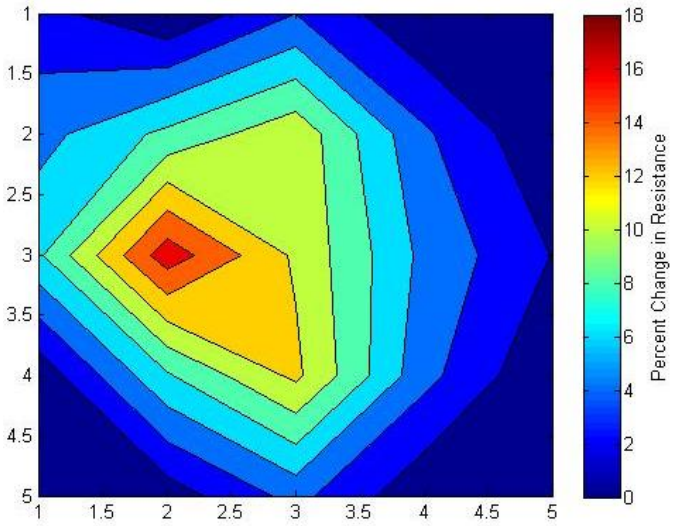

Figure 49 – First resistance peak of centered heater sine wave response.

This data shows a fairly symmetric resistance field with the exception of the sensitive R6 sensor located at (2,3). Other than a small skew in the center point, three of the corners show a similar gradient pattern. Again, the heater could have been a bit

off from center. The trend of the gradient, however, mimics the temperature distribution to which the sample was exposed quite well.

5.3 Corner Heater Results

The Peltier heater was moved to the upper left corner of the sensor grid to study how the sensors responded to a different temperature field. The placement of the heater and locations of the sensors and thermocouples can be found in Figure 50. According to the predicted temperature field and the calibration function, the sensors closer to the upper left should have a larger resistance response. The sensor pairs undergoing the same temperatures should ideally have the same resistance responses and are listed by largest expected response to smallest expected response: R1 and R3, R4 and R6, R2 and R8, R7 and R9, R5 and R11, and R10 and R12.

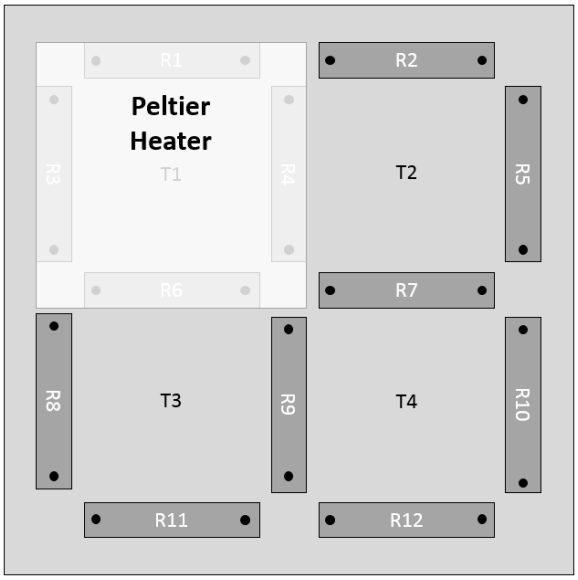

Figure 50 – Peltier heater placement and sensor diagram for corner heater experiment.

The results for the step function and sine wave experiments are presented in Section 5.3.1 and Section 5.3.2, respectively. These experiments were conducted on the same five grid samples that the centered heater experiments were run. The data

from the five samples were averaged for each of the twelve sensors to produce the percent resistance change responses presented in this section.

5.3.1 Step Function

The averaged signal from the twelve sensors to the step function can be seen in Figure 51.

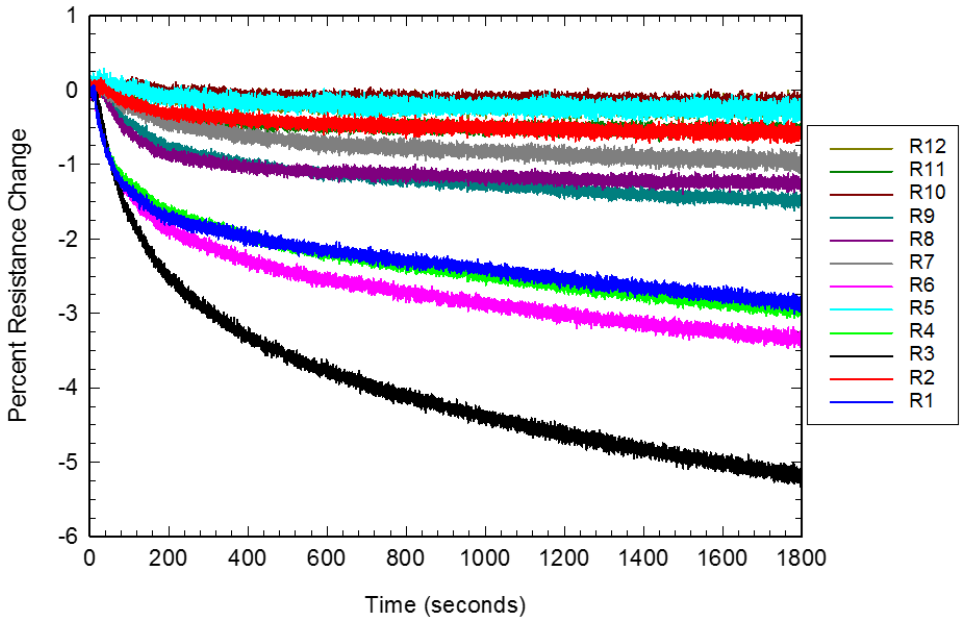

Figure 51 – Sensor grid resistance response to a temperature step function with a corner heater.

The sensors closest to the upper left corner exhibit a larger percent change in resistance over time than the sensors closest to the bottom right corner. A closer look at the more responsive sensors (R1, R3, R4, and R6) and the other eight less responsive sensors can be found separately in Figure 52 and Figure 53, respectively.

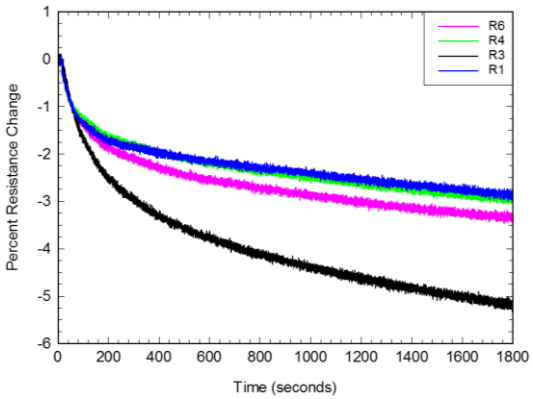

Figure 52 – Most responsive sensors to corner heater step function.

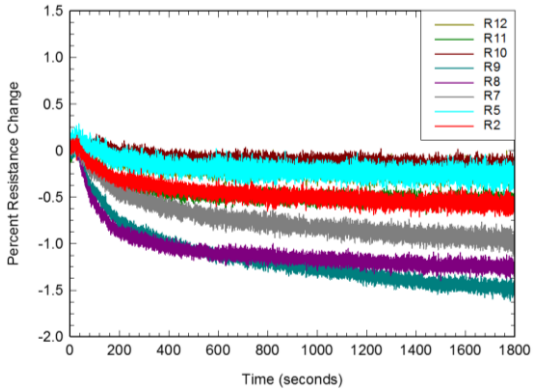

Figure 53 – Least responsive sensors to corner heater step function.

Sensors R1 and R4 are approximately equal, while sensor R6 has a slightly larger response and sensor R3 decreases about 2% more than the rest. Again, it seems as if sensor R3 is more sensitive, on average, than other sensors exposed to the same conditions. The responses graphed in Figure 53 show the expected resistance response behavior over the grid. For example, sensors R2, R7, R8, and R9 have a larger resistance change than R5, R10, R11, and R12. It should be noted that although theory says that the sensor pairs should have identical responses, there is some deviation in the experimental results.

Again, the resistance data from the last time step in this step function experiment was used to create a percent change in resistance contour plot and can be found in Figure 54.

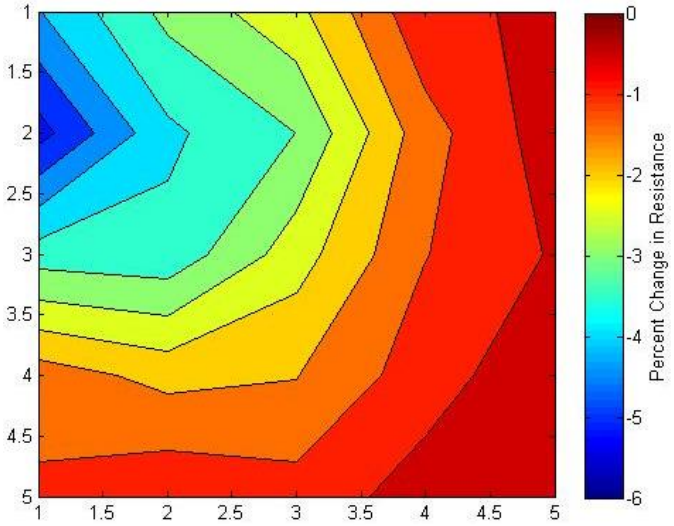

Figure 54 – Resistance response from end of corner heater step function response.

This resistance plot shows the same symmetry that the temperature field simulation predicts for a corner heat load with the exception of R3, located at (1,2). According to the calibration functions developed using the two-node samples, the blue areas should be the locations of the highest temperature whereas the red areas should be approximately room temperature. A better temperature calculation will be discussed in a later section.

5.3.2 Sine Function

The average responses to the sine wave heat load from each of the twelve sensors in the grid are presented in Figure 55. The same trends in responses from the pairs of sensors mentioned previously in Section 5.3.1 are expected for this experiment as well.

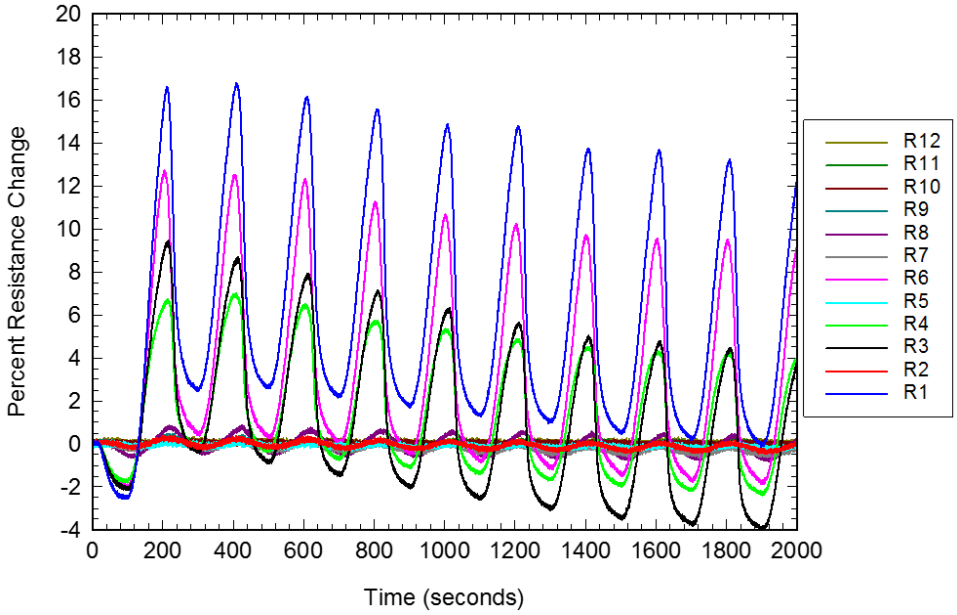

Figure 55 – Sensor grid response to a corner heater 5 mHz sine wave thermal load.

It is evident that sensors R1, R3, R4, and R6 are the most responsive because they are exposed to the highest temperature gradients during the experiment whereas the sensors exposed to the smallest temperature changes oscillate slightly around the initial resistance. A closer look for both sets of sensor responses can be found in Figure 56 and Figure 57.

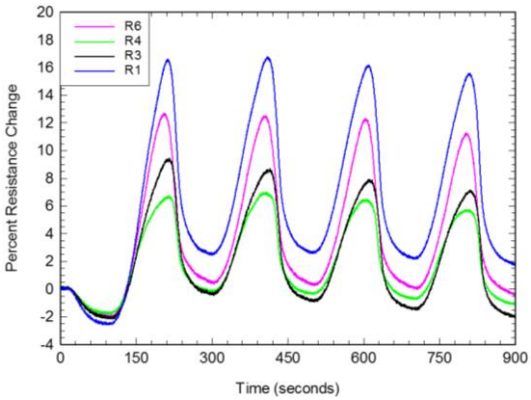

Figure 56 – Most responsive sensors to corner heater 5 mHz sine wave function.

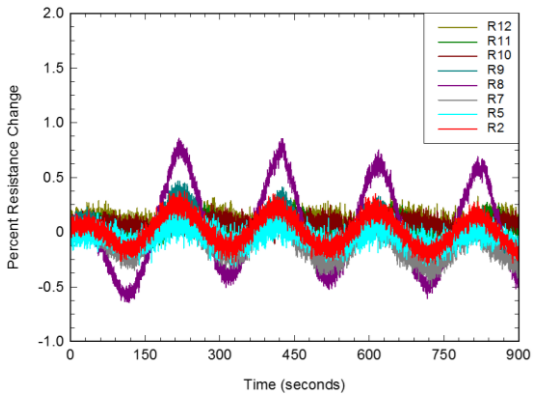

Figure 57 – Least responsive sensors to corner heater 5 mHz sine wave function.

Figure 56 shows that sensor R1 has the highest percent resistance change value for below room temperature (peaks in resistance response) and the above room

temperature portions (valleys in resistance response). The other three have varying peak resistance values but have approximately the same valley resistance. Figure 57 shows the expected trend that sensors R8 and R2 have a larger percent resistance change response than the furthest away sensors such as R10 and R12.

Just like the center sine wave experiment, the first resistance peak in this corner sine wave experiment was imported into the Matlab script to produce a contour plot of the percent change in resistance for temperatures below ambient. This plot can be found in Figure 58.

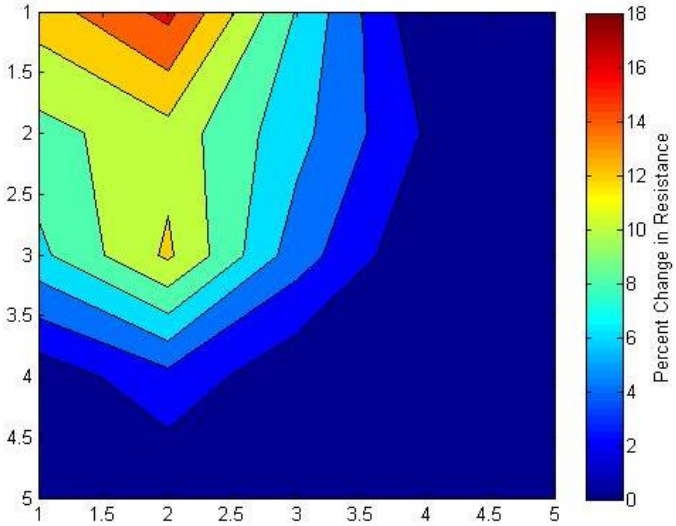

Figure 58 – First resistance peak from corner heater sine wave response.

This resistance field shows the expected corner symmetry but has a steeper gradient. There is much more substrate area that shows little to no resistance change. The next section will calculate the experimental temperature fields from the resistance contour plots.

5.4 Experimental Temperature Fields

The percent resistance changes for each of the twelve sensors in the grid samples were used to create contour plots for the step function and sine wave

experiments for heaters placed in the center and the corner of the grid samples. These resistances were converted into temperatures using the calibration functions established by the two-node samples. The temperature values taken by the four thermocouples during the experiments were used to compare the actual temperatures and the calculated values. The temperature contour plots can also be compared to the FEA simulation results. Figure 59 shows the data from the step function experiment with the heater in the center of the substrate.

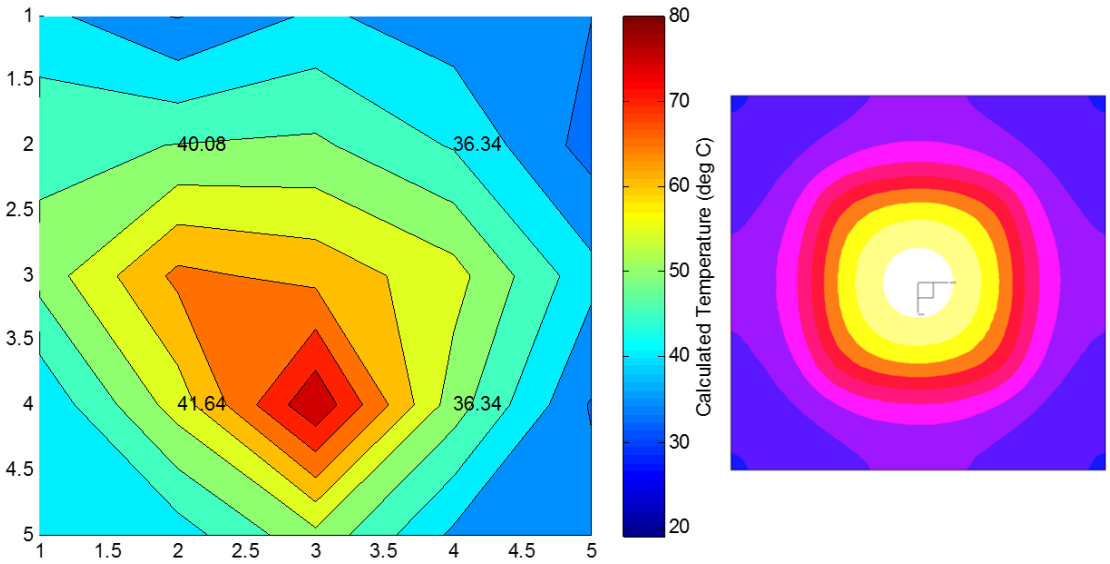

Figure 59 – (left) Calculated temperature field from centered heater experiment resistance field data and calibration function. (right) FEA temperature simulation result from before as a reminder.

The linear relationship was used to calculate the temperatures in this plot because it was above room temperature. The four values labeled on the contour plot reflect the actual thermocouple values. The top two thermocouple values are close to the value reflected by the colors of the contour. The bottom two values closest to the higher temperatures deviate more from the contour value. Despite being approximately 15 °C off from the calculated temperatures, the thermocouple readings do reflect the temperature distribution trend. The contour plot shows that the heater was slightly

southwest of center and the four thermocouple readings show that offset trend as well. All values can be compared to the FEA simulation provided in Figure 59 on the right. The thermocouple values align with the predicted values in the simulation plot.

The resistance data below room temperature from the sine wave experiment was converted into a temperature field using the exponential relationship established in the two-node sensor calibration. The temperature contour plot and the thermocouple values for this experiment can be found in Figure 60.

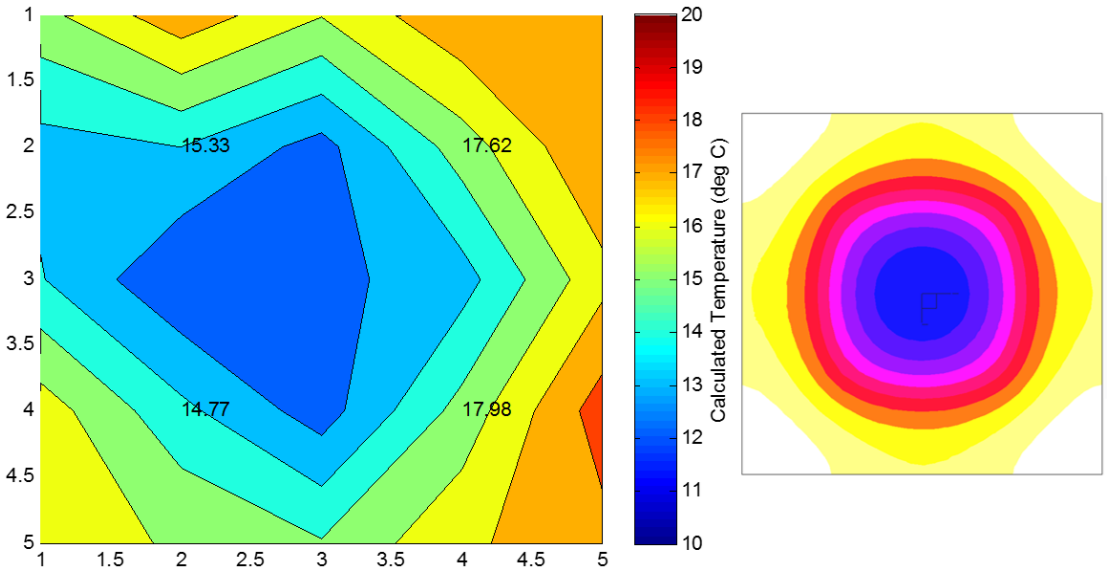

Figure 60 – (left) Calculated temperature field from centered heater experiment resistance field data and calibration function below room temperature. (right) FEA temperature simulation profile from before as a reminder.

The temperature contour plot values match the thermocouple values better than it did above room temperature. The lowest temperatures were measured by the two left thermocouples and the contour plot clearly shows that the Peltier heater must have been slightly left of center. The thermocouple values are only off by between 1 – 2 °C.

The corner heater experiment resistance data was also converted into temperature fields. The maximum temperatures reached were experienced in the step function experiment and are presented in Figure 61. Again, the four thermocouple

values are placed on the contours exactly where they were located on the substrate during the experiment.

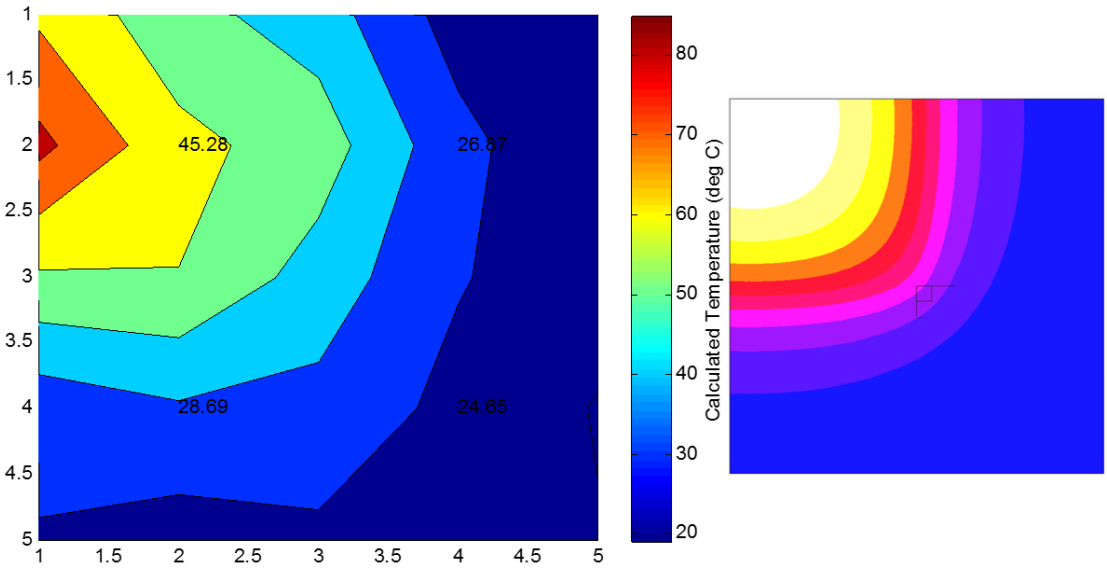

Figure 61 – (left) Temperature field for corner heater calculated using calibration function and resistance data from corner heater experiment. (right) FEA temperature simulation profile from before as a reminder.

The thermocouple values in Figure 61, except for the upper left, match the contour values within approximately 3-5 °C which is better than the difference found in the corresponding experiment with the centered heater. However, the upper left thermocouple value still deviates from the contour by approximately 15 °C. The values predicted in the FEA simulation reflect the values found in the contour plot. This difference could have been because sensor R3 seemed to be more sensitive than the others it was equal to, causing the calculated temperature at (1,2) to be higher than it should have been. Without this error, the gradient would have been smaller and the contour value would have been closer to the 45.28 °C that was measured by the thermocouple.

Finally, the corner heater sine wave resistance data was converted into temperatures using the exponential relationship. The temperature contour plot can be found in Figure 62.

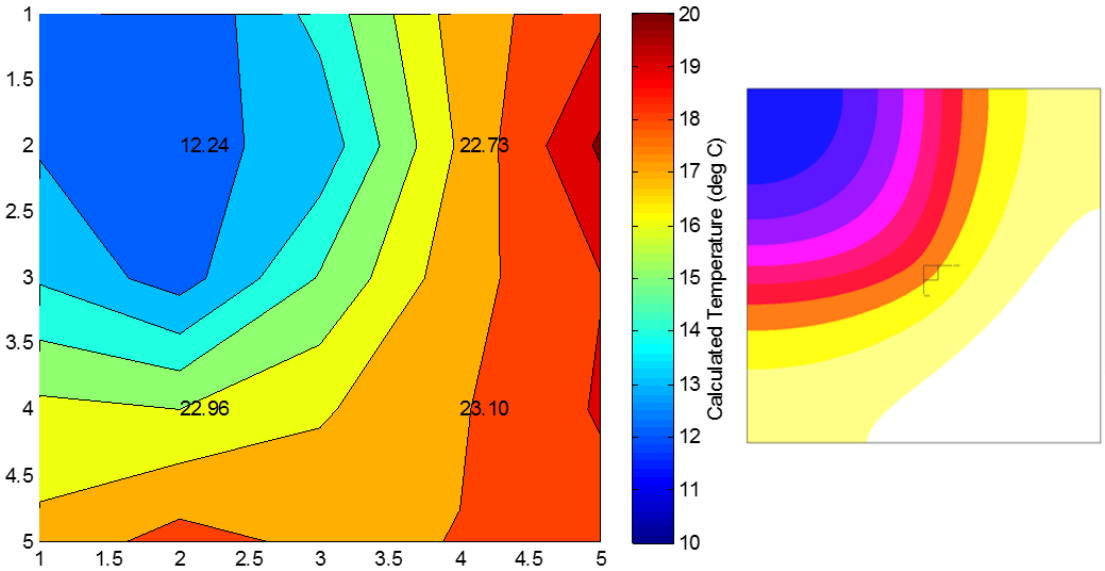

Figure 62 – (left) Calculated temperature field from corner heater experiment resistance field data and calibration function below room temperature. (right) FEA temperature simulation profile from before as a reminder.

The thermocouple directly over the heater accurately predicts the minimum temperature within a degree, which is the best correlation between contour and thermocouple values yet. However, the remaining three thermocouple values are about 5 °C higher than was calculated by the contours. This error is most likely due to the fact that the temperatures are close to room temperature. Because the trend below room temperature is exponential and the trend above room temperature is linear, temperatures around room temperature may be more difficult to predict.

5.5 Thermal Imaging Conclusions

The resistance fields generated from the twelve sensor grids were able to be converted into temperature fields using the calibration functions established previously.

These thermal images were compared to the thermocouple readings from the experiments as well as the FEA simulation temperature profiles.

The contour plots made from the data above room temperature deviated more from the thermocouple and FEA data than the plots made below room temperature. This is can be attributed to two causes. First, the calibration function below room temperature had smaller standard errors than the analysis above room temperature because of the outlier that was removed. It is also probably because below room temperature, there is a much smaller temperature range than there is above room temperature.

Another observation is that the thermal images produced for the corner heater experiments were closer to the thermocouple and FEA data. This is probably because it was much easier to be sure that the heater was placed in the corner of the substrate. The Peltier heater was aligned with both edges of the substrate. However, centering the heater was difficult because there was no reference point to align the heater with. Despite these issues, the twelve sensor grid samples were successful in reproducing the temperature profile shapes.

Chapter 6 – Conclusions

6.1 Two-Node Sensor Calibration

The two-node sensor calibration experiments investigated effects of the resistance response such as substrate CTE and EG loading. The substrate CTE affected the overall transient decrease in percent resistance change. However, this affect was unable to be quantified because the transient decrease varied too much between sensors on the substrate. Substrate-free sensors were made to investigate the temperature and resistance relationship of the EG and latex composite material without the effect of a substrate. The results of these experiments proved inconclusive because of the unavoidable strain applied during testing. Carbon fiber was chosen to conduct the calibration and grid sample experiments on because it is the substrate most likely to be found in the spacecraft.

The EG loading affected the "double hump" response found in the sine wave experiments. As EG loading increased, the "double hump" began to vanish. The 30 wt% sensor showed no "double hump" and was chosen for the calibration experiments. This "double hump" was modeled to show how three different functions were influencing the resistance response. The temperature verses percent resistance change was also modeled as a function of EG loading to predict when the graphite or percolation effects will dominate the bulk behavior. Calibration experiments were conducted on the 30 wt% sensors to characterize the temperature and percent resistance change above and below room temperature. Five identical two-node samples were made and averaged to get these calibration relationships.

This characterization of the EG and latex sensors on the carbon fiber substrate was used to produce thermal images over a surface. Twelve sensor grid samples produced resistance data over an area which could then be calculated into temperatures based on the relationships determined by the two-node sensors. Conclusions from the twelve sensor grid samples follow.

6.2 Twelve Sensor Grid

Twelve sensor grid samples were made and tested under two different temperature distributions. First, the heater was centered and the step function experiment and the sine wave experiment were conducted. The step function experiment showed a fairly symmetric resistance field but it seemed the heater may have been slightly below the center line. The sine function showed a particular sensitivity around R6 and the center of the response seemed to be slightly left of center. The corner heater experiment showed a step function response with a maximum resistance change around R3, however the resistance field was symmetric as expected. The sine wave response of the corner heater also showed a symmetric field with a little more response from R1 and R6.

These resistance fields from each of the four experiments on the twelve sensor grid samples were converted into temperature fields using the calibration functions established in the two-node sensor characterization experiments. The calculated temperature fields for each experiment were compared to the temperature values measured by the four T-type thermocouples placed during the experiments. The twelve sensor grid successfully mapped the temperature distribution trends but the values were slightly off. The thermal images were also compared to FEA simulations that

calculated the temperature distribution based on the heat load and convection condition. The plots below room temperature were predicted more accurately with the calibration than above room temperature.

6.3 Contributions

This research was conducted to achieve several goals, among which include material characterization above and below room temperature, calibration function development, and production of thermal images over the substrate. The experiments presented in this thesis were all used to reach those goals.

1. Percent resistance change was studied as a function of temperature, EG loading level, and substrate CTE in order to characterize the material. The EG loading and substrate were chosen from these experiments to be used in the development of the calibration models. These calibration models allowed the EG and latex composite to be used just as a traditional resistance-dependent temperature sensor like an RTD or thermistor would be. The conversion between resistance and temperature of these nano-filled composites based on particle resistance behavior and percolation theory is a novel step.

2. Twelve sensor grid samples were tested to measure the percent resistance change profile over the substrate surface. The calibration models were used to convert the resistance fields into temperature contours that were compared to thermocouple readings and FEA simulations. Although not perfect, the sensors successfully mapped the proper temperature trends over the surface. Further refinement of the calibration model will yield more accurate thermal images.

These thermal images, however, show for the first time that grids of nano-filled conductive polymer composites can predict temperatures over an area.

3. The ability to produce thermal images with these materials drastically improves upon the current thermal management systems in spacecraft. Although similar field data could be generated by a grid of thermocouples, the EG and latex sensors can be made in any shape to cover an adequate area. Next, the future work section discusses some next steps that will further enhance the future of these novel temperature sensors.

6.4 Future Work

There is some future work that would further the understanding of the EG and latex as a temperature sensor. Although the material was characterized experimentally, the physics on the nano-scale should be studied to exactly understand the interaction between the graphene particles and the latex matrix. We speculated each material's effect on the bulk response in this research but further understanding at the micro- and nano-scale is required before used in space.

The EG and latex resistance value was not reliably repeatable even when made in identical conditions. The variety between sensors is likely due to the random movement of the polymer chains in the latex because of the minimal crosslinking. A low crosslink density is desirable to yield compliance, however crosslinks are necessary to keep the chains in place. Other polymer materials should be studied for this application that are still compliant but have more crosslinking. Vulcanizing the latex is also an option to study the effects of these crosslinks.

The fact that these sensors have the potential to be 3-D printed onto a surface is very attractive to people in the spacecraft thermal management industry. Choosing a compatible polymer base material that can be used in 3-D printers is important for the future of this project. Three dimensional printing is the future of manufacturing processes and is being widely researched for spacecraft structures.

Finally, testing these sensors in a space environment will be crucial for the refinement of the sensor calibration. The resistance and temperature relationship of these materials could be different when under vacuum or in a sealed environment. These sensors could benefit spacecraft thermal management systems and should be continuously researched and developed.

Appendix A – Contour Plot Matlab Code

```
clc;clear
data=[time_step r1 r2 r3 r4 r5 r6 r7 r8 r9 r10 r11 r12];

R1=data(2); R2=data(3); R3=data(4); R4=data(5); R5=data(6);
R6=data(7); R7=data(8); R8=data(9); R9=data(10); R10=data(11);
R11=data(12); R12=data(13);

A=(R1+R3)/2;
B=(R1+R2+R4)/3;
C=(R2+R5)/2;
D=(R3+R6+R8)/3;
E=(R4+R6+R7+R9)/4;
F=(R5+R7+R10)/3;
G=(R8+R11)/2;
H=(R9+R11+R12)/3;
I=(R10+R12)/2;
J=(R1+R3+R4+R6)/4;
K=(R2+R4+R5+R7)/4;
L=(R6+R8+R9+R11)/4;
M=(R7+R9+R10+R12)/4;

X=[A R1 B R2 C;
R3 J R4 K R5;
D R6 E R7 F;
R8 L R9 M R10;
G R11 H R12 I];

contourf(X)
colorbar
caxis([0 18]) % Resistance Range [R_min R_max]
axis ij
ylabel(colorbar,'Percent Change in Resistance')
```

Bibliography

1. "Temperature measurements with thermocouples" (National Instruments, 2011).

2. S. A. Hill, C. K. B. Motil, W. Notardonato, S. Rickman, and T. Swanson, "Thermal Management Systems Roadmap Technology Area 14", edited by N. A. a. S. Administration (2012).

3. M. Kujawski, "Polymer Composites for Sensing and Actuation," Mechanical Engineering, University of Maryland, College Park (2011).

4. Spacecraft Thermal Control Handbook, Vol. 1, 2 ed. (The Aerospace Press, El Segundo, California, 2002).

5. "Space Mission Engineering: The New SMAD" in Space Technology Library, edited by J. R. Wertz, D. F. Everett, and J. J. Puschell (Microcosm Press, Hawthorne, CA, 2011).

6. R. Stierlin, J. Ricka, B. Zysset, R. Battig, H. P. Weber, T. Binkert, and W. J. Borer, "Distributed fiber-optic temperature sensor using single photo counting detection," Applied Optics, 26 (8)**,** 1368-1370 (1987).

7. H. A. Krishna, N. K. Misra, and M. S. Suresh, "Solar cell as a capacitive temperature sensor," IEEE Transactions on Aerospace and Electronic Systems, 47 (2)**,** 782-789 (2011).

8. I. Kang, M. J. Schulz, J. H. Kim, V. Shanov, and D. Shi, "A carbon nanotube strain sensor for structural health monitoring," Smart Mater. Struct., 15**,** 737-748 (2006).

9. H.-S. Chuang and S. Wereley, "Design, fabrication and characterization of a conducting PDMS for microheaters and temperature sensors," Journal of Micromechanics and Microengineering, 19 (4)**,** 7 (2009).

10. M. Kujawski, J. D. Pearse, and E. Smela, "Elastomers Filled with Exfoliated Graphene as Compliant Electrodes," Carbon, 48**,** 2409 - 2417 (2010).

11. J. Wissman, A. Perez-Rosado, A. Edgerton, B. M. Levi, Z. N. Karakas, M. Kujawski, A. Philipps, N. Papavizas, D. Fallon, H. A. Bruck, and E. Smela, "New Compliant Strain Gauges for Self-Sensing Dynamic Defomation of Flapping Wings on Miniature Air Vehicles," Smart Mater. Struct., 22 (2013).

12. R. Strumpler, "Polymer composite thermistors for temperature and current sensors," Journal of Applied Physics, 80 (11)**,** 6091-6096 (1996).

13. T. A. Kim, H. S. Kim, S. S. Lee, and M. Park, "Single-walled carbon nanotube/silicone rubber composites for compliant electrodes," Carbon, 50**,** 444-449 (2012).

14. M. A. Osman and D. Srivastava, "Temperature dependence of the thermal conductivity of single-wall carbon nanotubes," Nanotechnology, 12**,** 21-24 (2001).

15. P. A. Kinzie, Thermocouple Temperature Measurement, (John Wiley & Sons, 1973).

16. L. Michalski, K. Eckersdorf, and J. McGhee, Temperature Measurement, (John Wiley & Sons, England, 1991).

17. R. A. Matula, "Electrical resistivity of copper, gold, palladium, and silver," Journal of Physical and Chemical Reference Data, 8 (4)**,** 1147-1298 (1979).

18. J. S. Steinhart and S. R. Hart, "Calibration curves for thermistors," Deep-Sea Research and Oceangraphic Abstracts, 15**,** 497-503 (1968).

19. Z. Spitalsky, D. Tasis, K. Papagelis, and C. Galiotis, "Carbon nanotube-polymer composites: chemistry, processing, mechanical and electrical properties.," Progress in Polymer Science, 35**,** 357-401 (2010).

20. A. Yu, P. Ramesh, X. Sun, E. Bekyarova, M. E. Itkis, and R. C. Haddon, "Enhanced Thermal Conductivity in a Hybrid Graphene Nanoplatelet - Carbon Nanotube Filler for Epoxy Composites," Advanced Materials, 20**,** 4740 - 4744 (2008).

21. V. C. Tung, L.-M. Chen, M. J. Allen, J. K. Wassel, K. Nelson, R. B. Kaner, and Y. Yang, "Low-temperature solution processing of graphene-carbon nanotube hybrid materials for high-performance transparent conductors," Nano Letters, 9 (5)**,** 1949-1955 (2009).

22. C. H. Liu, H. Huang, Y. Wu, and S. S. Fan, "Thermal conductivity improvement of silicone elastomer with carbon nanotube loading," Applied Physics Letters, 84 (21)**,** 4248-4250 (2004).

23. N. Hu, Y. Karube, C. Yan, Z. Masuda, and H. Fukunaga, "Tunneling effect in a polymer/carbon nanotube nanocomposite strain sensor," Acta Materialia, 56**,** 2929-2936 (2008).

24. N. C. Das, T. K. Chaki, and D. Khastgir, "Effect of processing parameters, applied pressure and temperature on the electrical resistivity of rubber-based conductive composites," Carbon, 40**,** 807-816 (2002).

25. C. Zhang, C.-A. Ma, P. Wang, and M. Sumita, "Temperature dependence of electrical resistivity for carbon black filled ultra-high molecular weight polyethylene composites prepared by hot compaction," Carbon, 43**,** 2544-2553 (2005).

26. U. Khan, P. May, A. O'Neill, and J. N. Coleman, "Development of stiff, strong, yet tough composites by the addition of solvent exfoliated graphene to polyurethane," Carbon, 48**,** 4035-4041 (2010).

27. J. R. Potts, D. R. Dreyer, C. W. Bielawski, and R. S. Ruoff, "Graphene-based polymer nanocomposites," Polymer, 52**,** 5-25 (2011).

28. K. Ohe and Y. Naito, "A new resistor having an anomalously large positive temperature coefficient," Japanese Journal of Applied Physics, 10 (1) (1971).

29. M. Hernandez, M. d. M. Bernal, R. Verdejo, T. A. Ezquerra, and M. A. Lopez-Manchado, "Overall performance of natural rubber/graphene nanocomposites," Composites Science and Technology, 73**,** 40-46 (2012).

30. I. M. Afanasov, V. A. Morozov, A. V. Kepman, S. G. Ionov, A. N. Seleznev, G. V. Tendeloo, and V. V. Avdeev, "Preparation, electrical and thermal properties of new exfoliated graphite-based composites," Carbon, 47**,** 263-270 (2009).

31. T. Kuilla, S. Bhadra, D. Yao, N. H. Kim, S. Bose, and J. H. Lee, "Recent advances in graphene based polymer composites," Progress in Polymer Science, 35**,** 1350-1375 (2010).

32. Y. Zhou, F. Pervin, V. K. Rangari, and S. Jeelani, "Fabrication and evaluation of carbon nano fiber filled carbon/epoxy composite," Materials Science and Engineering A, 426**,** 221-228 (2006).

33. S. Ganguli, A. K. Roy, and D. P. Anderson, "Improved thermal conductivity for chemically functionalized exfoliated graphite/epoxy composites," Carbon, 46**,** 806-817 (2008).

34. Y. X. Zhou, P. X. Wu, Z.-Y. Cheng, J. Ingram, and S. Jeelani, "Improvement in electrical, thermal and mechanical properties of epoxy by filling carbon nanotube," eXPRESS Polymer Letters, 2 (1)**,** 40-48 (2008).

35. Y.-H. Liao, O. Marietta-Tondin, Z. Liang, C. Zhang, and B. Wang, "Investigation of the dispersion process of SWNTs/SC-15 epoxy resin nanocomposites," Materials Science and Engineering A, 385**,** 175-181 (2004).

36. Z.-K. Chen, J.-P. Yang, Q.-Q. Ni, S.-Y. Fu, and Y.-G. Huang, "Reinforcement of epoxy resins with multi-walled carbon nanotubes for enhancing cryogenic mechanical properties," Polymer, 50**,** 4753-4759 (2009).

37. C. Cochrane, V. Koncar, M. Lawandowski, and C. Dufour, "Design and development of a flexible strain sensor for textile structures based on a conductive polymer composite," Sensors, 7**,** 473-492 (2007).

38. S. Kirkpatrick, "Percolation and conduction," Reviews of Modern Physics, 45 (4)**,** 574-588 (1973).

39. A. Rudin, The elements of polymer science and engineering, 2 ed. (Academic Press, San Diego, CA, 1999).

40. D. D. L. Chung, "Review Graphite," Journal of Materials Science, 37**,** 1475-1489 (2002).

41. , ArtMolds, "Technical bulletin: 407 latex slip casting latex", http://www.artmolds.com/media/blfa_files/Tech_407_LATEX.pdf.

42. E. H. L. Falcao, R. G. Blair, J. J. Mack, L. M. Viculis, C.-W. Kwon, M. Bendikov, R. B. Kaner, B. S. Dunn, and F. Wudl, "Microwave exfoliation of a graphite intercalation compound," Carbon, 45**,** 1364-1369 (2007).

43. T. Wei, Z. Fan, G. Luo, C. Zheng, and D. Xie, "A rapid and efficient method to prepare exfoliated graphite by microwave irradiation," Carbon, 47**,** 313-347 (2008).